Flexible-Cost SLAM

by

Matthew Koichi Grimes

A dissertation submitted in partial fulfillment

of the requirements for the degree of

Doctor of Philosophy

Department of Computer Science

New York University

May 2012

Professor Yann LeCun

For Lyubashka.

Acknowledgements

My parents come first in this list of thanks, for their support. My friend Yotam comes second, for his example.

Thanks to my history of professors, who have channeled my progress: Nancy Pollard, Greg Turk, Aaron Bobick, Jovan Popovic, Takeo Igarashi, and finally, Yann.

This thesis was written in a nomadic state across three cites and two coasts. Thank you to Gail Baugh and Jim Warshell for their opening their home to me in San Francisco. Thanks to the cafes Diesel and TrueGrounds, the Tisch Library at Tufts, and the Physics Reading Room at MIT, for providing a daily desk to a stranger. Thanks to Flying Lotus for the soundtrack, and Lenovo for a long-lasting battery.

While not a professor, no person has helped me more with the nuts and bolts of writing code than Drago Anguelov of Google, whose perfectionism and generous contributions of data went well above the call of duty of an ex-boss. This thesis, and my work in general, has benefitted immeasurably.

Finally, thank you to my wife Lyuba, with whom all is possible.

Abstract

The ability of a robot to track its position and its surroundings is critical in mobile robotics applications, such as autonomous transport, farming, search-and-rescue, and planetary exploration.

As a foundational building block to such tasks, localization must remain reliable and unobtrusive. For example, it must not provide an unneeded level of precision, when the cost of doing so displaces higher-level tasks from a busy CPU. Nor should it produce noisy estimates on the cheap, when there are CPU cycles to spare.

This thesis explores localization solutions that provide exactly the amount of accuracy needed to a given task. We begin with a real-world system used in the DARPA Learning Applied to Ground Robotics (LAGR) competition. Using a novel hybrid of wheel and visual odometry, we cut the cost of visual odometry from 100% of a CPU to 5%, clearing room for other critical visual processes, such as long-range terrain classification. We present our hybrid odometer in chapter 2.

Next, we describe a novel SLAM algorithm that provides a means to choose the desired balance between cost and accuracy. At its fastest setting, our algorithm converges faster than previous stochastic SLAM solvers, while maintaining significantly better accuracy. At its most accurate, it provides the same solution as exact SLAM solvers. Its main feature, however, is the ability to flexibly choose any point between these two extremes of speed and precision, as circumstances demand. As a result, we are able to guarantee real-time performance at each timestep on city-scale maps with large loops. We present this solver in chapter 3, along with results from both commonly available datasets and Google Street View data.

Taken as a whole, this thesis recognizes that precision and efficiency can be competing values, whose proper balance depends on the application and its fluctuating circumstances. It demonstrates how a localizer can and should fit its cost to the task at hand, rather than the other way around. In enabling this flexibility, we demonstrate a new direction for SLAM research, as well as provide a new convenience for end-users, who may wish to map the world without stopping it.

Contents

List of Appendices

List of Figures

List of Tables

1 Introduction

Unlike other areas in computer science, mobile robotics has not generally enjoyed an overabundance of processing power. This is sometimes the result of designing hardware for physical robustness over speed. For example, the Mars Exploration Vehicle's CPU is made resistant to radiation and draws little power, in exchange for running at a mere 20 MHz [33]. At other times, the burden of processing high-dimensional sensor input (e.g. video) at real-time rates can leave little processor time for anything else. Finally, and most cripplingly, human ambition for robotics as a field currently far outstrips its fledgling capabilities. If for no other reason, it seems safe to assume that this last factor will keep robot processors running at capacity for years to come.

Localization and SLAM is considered a maturing field, at least within the static-world assumption. The current minimum bar for publication seems to be set at real-time operation in three-dimensional, building-sized environments, and this standard is rising rapidly. From the vantage point of this plateau, however, we may see that many real engineering problems have been left unaddressed.

For one, the term "real-time" is often used in the weaker sense of *amortized* real-time performance, wherein saturating the CPU for two full seconds can be forgiven, so long as it is left unmolested for the next ten. This standard is insufficient for even moderately complex systems, which will have critical components competing with SLAM for immediate CPU time. One may lessen the blow by running the localizer in a low-priority thread, but this introduces problems of its own. For example, delaying large corrections to the robot location can disrupt dependent systems such as landmark recognition and navigation. Therefore, the preferable standard to amortized real-time performance is *guaranteed* real-time performance, wherein the localizer can always process a frame's sensor input well before the next frame, even in the worst case. In chapter 3 we demonstrate a system that maintains this guarantee even in city-scale environments.

Another practical concern left largely unaddressed is that optimal precision is often not worth its cost. In chapter 2 we present a frugal visual odometry solution that delivers 95% cost savings over conventional VO by estimating only rotation, leaving translation to be efficiently measured by wheel odometry. While less accurate than a full visual odometer, our system nonetheless delivers comparable accuracy over moderate distances, while freeing up CPU time for a long-range visual traversability classifier. In off-road navigation, long-range vision is far more valuable than pixel-perfect local accuracy. This trade-off would have been impossible under a short-sighted commitment to optimal local precision.

There are exact SLAM solvers, and faster but more approximate SLAM solvers. What these both presume is that which is more desirable will not change during the lifetime of the robot. This is often untrue. The amount of available CPU cycles can fluctuate sharply from frame to frame, due to the unpredictable demands of other components as they respond to a dynamic environment. One would therefore prefer to be able to choose the amount of time to spend on localization, where more time translates to more precision. Chapter 3 describes a novel SLAM algorithm with flexible cost. It will process the sensor input of a frame within a dynamically chosen budget, which may range from $O(N)$ to $O(N^2)$ in the size of the loop to be closed.

Finally, many SLAM papers demonstrate "real-time operation" empirically, by showing acceptable performance on established datasets. However, this performance is often the result of using limited-range sensors such as laser scanners, or operating indoors, where loop sizes are small. This experimental validation leaves some of these SLAM solvers less than future-proof against large loops, and impending contributions from computer vision, such as long-range landmark recognition. Both of these can play a large part outdoors. In chapter 3 we demonstrate how to guarantee real-time performance bounds even in the face of such locally dense graphs and large loops.

Taken together, these chapters describe localization solutions which save significant amounts of computation over competing methods, by delivering a level of precision appropriate to the task at hand. The saved cost can be used on additional components whose value far exceeds that of an incremental increase in precision. Furthermore, by making the cost adjustable, the H_2O solver allows as much precision as the robot can afford, thus providing an unobtrusive and reliable bedrock upon which to build complex mobile systems.

2

Efficient Off-Road Localization with Visually Corrected Odometry

We describe an efficient, low-cost, low-overhead system for robot localization in complex visual environments. Our system augments wheel odometry with visual orientation tracking to yield localization accuracy comparable with “pure” visual odometry at a fraction of the cost. Such a system is well-suited to consumer-level robots, small form-factor robots, extraterrestrial rovers, and other platforms with limited computational resources. Our system also benefits high-end multi-processor robots by leaving ample processor time on all camera-computer pairs to perform other critical visual tasks, such as obstacle detection. Experimental results are shown for outdoor, off-road loops on the order of 200 meters. Comparisons are made with corresponding results from a state-of-the-art pure visual odometer.

2.1 Introduction

The ability for a robot to localize itself can be critical for successful autonomous operation. While a globally consistent solution to the localization problem must necessarily also perform mapping [48], many applications do not require or benefit from a globally consistent map. Locally consistent approaches such as fixed-time-window SLAM [4] and visual odometry [1, 35] have shown great success in applications such as goal-directed navigation and localization in dynamic environments.

Wheel odometry has been a popular mainstay for robotic localization due to its low overhead and high sampling frequency. Its accuracy however is limited by wheel slip, a source of error that can be challenging to detect and correct without other sensors. Wheel slip can be particularly frequent and destructive in runs over outdoor terrain with loose or uneven ground. Full visual odometry (VO) uses feature tracking to entirely replace ground odometry, but current systems [1] require 100% of the processing time on a high-end CPU. For single-CPU autonomous robots, this cost can be prohibitive. The cost of VO can be a burden even for multi-CPU platforms, as it is often desirable for all camera-computer pairs to be able to perform additional tasks, such as short-range obstacle detection, at high framerates in their respective fields of view.

We have implemented a visual localization system that runs at a fraction of the cost of state-of-the-art VO systems while maintaining comparable accuracy. On our multi-processor, multi-camera system, this allows a single processor-camera pair to handle VO in parallel with other visual tasks, enabling tight coupling between localization, obstacle detection, and control. Our system can be of even more use to robots with limited computational power, such as small robots, consumer-oriented platforms, or extraterrestrial rovers.

We achieve this performance gain by specializing the visual odometer to the task of tracking only one degree of freedom: the robot's bearing. This bearing estimate is combined with a wheel odometer's translation estimate to yield 3-DOF pose estimates with much-improved accuracy over wheel odometry, and comparable accuracy to 6-DOF visual odometers on low-curvature terrain. The efficiency of our system comes from the fact that tracking only the bearing allows us to operate at much lower resolutions than would be acceptable on a 6-DOF odometer. This is because the uncertainty of an object's distance grows rapidly with distance at low resolutions, while the uncertainty of its robot-relative bearing is constant. For example, at our resolution of 160x120 pixels, an uncertainty of ± 0.25 pixels translates to ± 0.1 degrees of yaw, but ± 1.25 meters of distance for an object 6 meters away. Additional speedups are gained by using spherical image projection for more reliable feature tracking, and limiting the feature tracking to windows bounded by wheel odometer output. We show that this hybrid odometry approach achieves much of the benefit of a full visual odometer at a greatly reduced computational cost.

2.2 Related Work

There has been much work in both wheel odometry and visual odometry (VO), while only limited attention has been paid to the intersection of the two approaches. Schaefer et. al. [43] use wheel odometry to check the output of a full VO system for errors arising from moving objects. Similarly, Kneip et al use inertial sensors to provide a motion prior to increase the robustness of full VO [30]. Rather than run full VO in parallel to wheel odometry or inertial sensors, we have focused on how to best exploit wheel odometry to lighten the computational burden of VO. A number of authors have used visual matching to correct IMU or GPS data on aerial platforms [6] [3] [49]. Our system is implemented on a ground rover, where many of the assumptions afforded in the air, such as nearly coplanar features and slow visual flow, do not apply.

Most other work in relative pose tracking has focused either on using non-visual sensors to detect wheel slip, or on employing full visual odometry as a complete replacement to wheel odometry.

2.2.1 Wheel odometry correction

Wheel slip can occur in many flavors, from sudden spurts of wheel speed to gently increasing drift. The latter in particular is difficult to detect by simple cross-checking against motor current or inertial sensor output, requiring more nuanced approaches. Ojeda et. al. [36] correct odometry using parametrized functions of motor current and soil cohesion. However, Maimone et. al. [33] report that such an approach fares poorly unless the soil consistency is nearly homogeneous. Ward and Iagnemma train an SVM on hand-labeled odometric and inertial sensor outputs to detect immobilization [51]. In another paper [52], the same authors employ a model-based approach, inferring robot velocity by fusing the output of a physical model with IMU, GPS, and wheel odometry output. A simpler approach to detecting slip would be to complement odometry with the absolute position measurements provided by GPS. Unfortunately, GPS input can be sporadic and inaccurate in wooded or urban environments [41] [23]. Even in open fields, typical refresh rates are around once per second [13]. On our ground rover platform, we have found that one second is plenty of time for a robot to hallucinate a sharp turn due to wheel slip and react by sharply turning in the opposite direction. When driving alongside entangling vegetation or on narrow forest paths, such sudden "corrective" turns can prove catastrophic to a run. Furthermore, both GPS and odometry exhibit highly non-Gaussian error profiles, as neither GPS "jumps" nor wheel slip errors are well modeled as a random walk around a mean value. Sukkarieh et. al. [41] therefore use a chi-squared gating function to detect and discard blatantly spurious sensor outputs, and feed only vetted sensor readings to a Gaussian model, in their case an EKF sensor fusion algorithm. However, this does not address the problem of GPS's low update frequency, nor a gating function's insensitivity to gradual odometry drift at low speeds. Rather than attempting to selectively detect and correct bad rotation estimates by the wheel odometer, we have opted to replace them entirely with the more reliable rotation estimates of our visual rotation tracker.

2.2.2 Full visual odometry

Full visual odometry tracks visual features to make a differential estimate of the robot's full 6-DOF pose. Moravec pioneered the approach in 1980, with his work on the Stanford cart [34]. Nistér et. al. [35] tracked Harris corners [19] in real time, discarding spurious feature associations between frames using RANSAC [12]. Others have used the more recent FAST feature detector [40] in place of Harris corners. Alternatives to RANSAC include graph-based consistency checking [24] and exploiting the camera platform's motion constraints [42]. Huang et. al. used an RGBD camera to provide input to a VO system [25], whereas we used a stereo camera, which is more appropriate for outdoor use. Agrawal et. al. boosted accuracy by incorporating bundle adjustment to reduce drift [1]. However, their system occupies all of the processor time on a high-end CPU, requiring additional computers to handle other aspects of autonomous operation such as mapping and planning. The NASA Mars Exploration Vehicle is hit particularly hard by the computational demands of full VO, which can take up to 3 minutes per frame on its 20 MHz processor, leading to an average movement of 10m/hour [33]. By contrast, our system is implemented on the same robotic platform used in [1] where one of its two camera-computer pairs is dedicated to the task of real-time full VO. However, this leaves that camera-computer pair unable to perform other potentially critical tasks on its field of view, such as obstacle detection. For this reason, we have chosen our more lightweight approach. Kaess et al exploit the same core observation that we do, namely that faraway features are useful for estimating rotation, while nearby features are better for estimating translation [28]. They exploit this observation to increase robustness to degenerate input, while we use it to increase speed.

2.3 Algorithm

In the interest of keeping running costs down, our system tracks only six patches per frame, tracking wide image patches at low resolution. The system samples patches from a region around the horizon, interpreting their horizontal motion from frame to frame as a rotation of the robot. There are two challenges to this approach: one is that a small number of features may be less robust to mismatches. The other is that a robot driving in a straight line will see features drift towards the sides of the image as it drives by ("parallax drift"). Under a naïve implementation, such horizontal motion in the image would be incorrectly interpreted as a rotation. In this section we give a walkthrough of our algorithm, paying particular attention to the solutions to the above problems. The overall algorithm is as follows:

1. Re-map the image to remove feature size distortions due to planar projection.
2. Sample features from a small region of the previous frame selected using wheel odometry.
3. Search for the sampled features in the current frame, again limiting the search area using wheel odometry.
4. Cross-validate the features' motions between frames and discard any outliers.
5. Localize the robot in the current frame by replacing the wheel odometry's rotation estimate with that of the visual odometer, and rotating the translation estimate by the difference in rotations.

While the sampling and searching steps above use wheel odometry, they do so in a manner that is not adversely affected by wheel slip, as will be discussed in section 2.3.3.

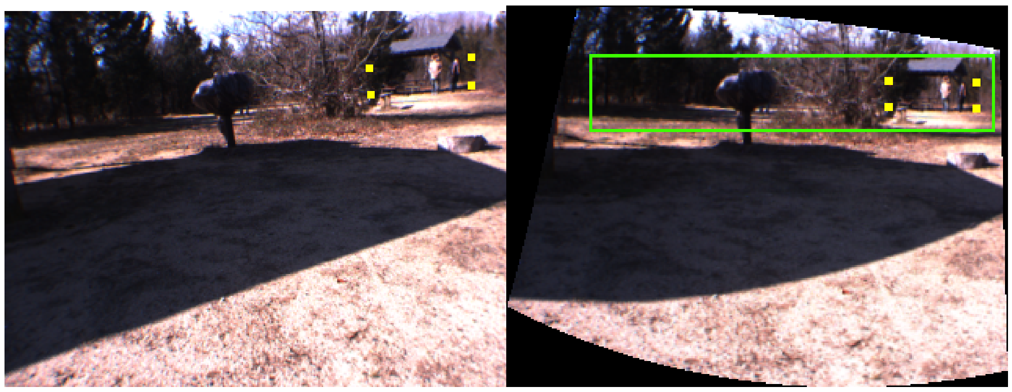
(a) Camera image (b) Spherical image

Figure 2.1: A rectified camera image and its spherical transform. The asymmetry of the spherical image is due to the fact that the camera is pointed off to the left and down, with some axial roll. The robot is pointed straight at the area highlighted by four yellow dots, placed at pitch and yaw values $[0.03, 0.1]$, $[0.03, -0.1]$, $[-0.03, -0.1]$, and $[-0.03, 0.1]$, in radians. After the transformation, these points form an axis-aligned rectangle around the frontal direction. In practice, we transform only the portion of the camera image roughly located around the horizon, highlighted by the green rectangle above.

2.3.1 Re-map image to a spherical projection

Because we track a small number of image patches per frame, care must be taken to minimize the number of mismatched patches. We use wide patches subtending eight degrees of yaw, as larger patches tend to be more distinctive. However, such large features stretch when moved from the center of the image to the edges, where each pixel subtends a smaller solid angle. This distortion can cause mismatches when searching for features that have moved from the center of the image to near an edge, or vice-versa. To remove this distortion, we remap the camera image using a "spherical projection", where each pixel row and column covers a fixed amount of vehicle-relative pitch and yaw $[\phi_p, \theta_p]$, respectively (figure 2.1). We define the mapping from camera image coordinates $[i, j]$ to spherical image

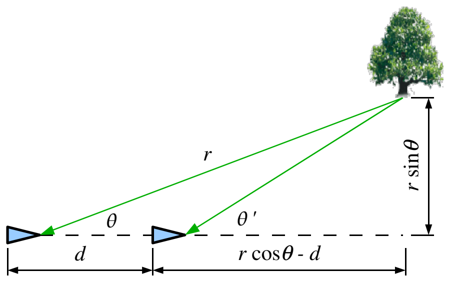

Figure 2.2: **Parallax from pure forward motion.** We wish to limit our attention to objects which will not shift under parallax from frame to frame. In a spherical image where each pixel subtends θ_p radians of yaw, this requires that the bearing θ of the object not change more than $\theta_p/2$. Given upper limits on θ and the frame-to-frame translation d, we may solve for a minimum distance r. We avoid parallax by detecting distance using stereo data calculated earlier for obstacle detection, and ignoring all features closer than r.

coordinates $[k, l]$ as:

$$k(i,j) = (\phi(i,j) - \phi_o)/a \tag{2.1}$$

$$l(i,j) = (\theta(i,j) - \theta_o)/a \tag{2.2}$$

Here, a is a chosen ratio of radians per pixel, and $[\phi_o, \theta_o]$ is the pitch and yaw of the view ray corresponding to the upper-left pixel in the spherical image. We choose a as being the radians-per-pixel of the center pixel in the planar image. We perform this mapping using a precalculated coordinate look-up table.

2.3.2 Sampling features

Even when the robot is moving straight forward, any feature except for those directly in front of the robot will experience nonzero drift towards the side of the image as the robot drives by. If we are to interpret the horizontal motion of features as robot rotation, we must limit our features to those for which this frame-to-frame “parallax drift” is less than half a pixel in the spherical image, and therefore undetectable. As shown in figure 2.2, this constraint defines a minimum value for a feature’s distance r as a function of its bearing θ, the maximum possible travel of the camera between frames d, and the yaw subtended by a pixel in the spherical image θ_p:

$$r_{min} = \frac{d \tan(\theta_p/2 + \theta)}{\cos\theta \tan(\theta_p/2 + \theta) - \sin\theta} \tag{2.3}$$

With a sufficiently reliable stereo vision system with which to estimate r, one could threshold all features in the image by their distance. However, the threshold r_{min} increases with bearing θ, and stereo depth is unreliable for faraway features at low image resolutions. We therefore opt to limit our sampling to a small range of yaw $-\theta_{max} < \theta < \theta_{max}$ centered on the frontal direction $\theta = 0$. We then substitute θ_{max} for θ in equation 2.3 to derive a corresponding minimum distance r_{min}. Any feature closer than r_{min} is deemed unfit for use. When an insufficient number of viable landmarks are found in a particular frame, the pose for that frame is estimated using wheel odometry. In practice, this happens relatively rarely outdoors. Even in dense forests such as the one in figure 2.4c, the many nearby obstacles (trees) caused our hybrid VO system to defer to wheel odometry on only 7.9% of the frames. We found that this was sufficiently low to maintain good performance on uneven and slippery forest ground. Two exceptions where distal features may be intermittent are areas that are dense with eye-level vegetation, or extremely hilly areas where the terrain regularly rises to eye level within r_{min} meters. The former situation can be mitigated by slowing down to reduce d, and therefore reduce r_{min}, when VO finds itself frequently delegating to wheel odometry. The latter case of severely hilly terrain presents mapping difficulties for any 3-DOF model, though our visual tracker still presents an improvement over wheel odometry for control purposes.

On our system, we estimate distance using the dense stereo image already calculated by another component for the purposes of obstacle detection. If no such calculation is already being done, the approach of [1] may be used, where stereo disparity is calculated for each patch rather than for all pixels. Our use of stereo information is distinguished by its low requirement for depth precision. We need only establish whether a patch is close enough to drift due to parallax between neighboring frames. The lower the resolution, the looser this requirement becomes, as features need to drift farther to cause noticeable pixel shift. This low dependence on depth precision enables our method to operate efficiently on low resolution video. By contrast, pure VO methods that use the depth estimate to measure translation are more sensitive to the high depth uncertainty at low image resolutions.

The choice of θ_{max} can be made based on the robot's expected speed, environment, and camera geometry. On our platform, the cameras point off to the sides, thereby making the frontal direction close to one side of the spherical image (see figure 2.1b). We therefore chose θ_{max} to be the absolute value of the yaw of that side, namely ± 0.09 or ± 0.14 radians depending on the eye. This left 15% to 23% of the horizon image available for sampling. Using these θ_{max} values, along with a d of 0.13 meters (1.3 m/s / 10 Hz), equation 2.3 yields minimum distances r_{min} of 2.42m and 3.69m.

The region defined by $-\theta_{max} < \theta < \theta_{max}$ is further shrunk on all sides by half the patch dimensions before searching for Harris corners in one of its channels.

These corners are used to find suitable points from which to sample RGB patches. The shrinkage is done to ensure that patches centered on these corners are completely contained within $-\theta_{max} < \theta < \theta_{max}$. The horizon images labeled "previous frame" in figure 2.3 show this region in blue. As each image patch is selected, the Harris corners under that patch are set to zero as a form of non-max suppression. We sample 6 patches measuring 13 x 3 pixels, or 7.6 by 1.75 degrees of solid angle, or 11% by 3% of the field of view. Note that while we sample in a narrow region, the search region is not so constrained. Therefore, θ_{max} does not present a limit on our robot's rotation rate.

2.3.3 Searching for patches

In outdoor environments, it is a common occurrence for the robot to rotate less than reported by wheel odometry ("wheel slip"). The opposite case of the robot rotating significantly more than the wheels ("wheel skid") is far less common under vehicle speeds typically operated under by autonomous vehicles [52]. We therefore trust our odometry to set an upper limit on the expected patch motion from frame to frame. Vehicles that do operate at skid-inducing speeds may choose to employ low-resolution whole-image matching, used by Klein et al [29] for efficient high-speed tracking, to provide another prior for the patch locations. When searching for image patches, we limit our search window to a region that encompasses the patch's position in the previous frame and the patch's position in the current frame, as predicted by wheel odometry. This window is inflated on all sides by half the patch dimensions for an added measure of safety. We apply a normalized cross-correlation of the image patch with this search window, and choose the maximum as the best-matching location.

On our platform, the camera used for VO points off to one side, putting the frontal direction near the side of the image. Features sampled from this area are easily scrolled off that frontal side of the screen when the robot turns away from it. We therefore choose the sampling location using wheel odometry. If it indicates a turn away from the frontal side, we sample not from the previous image's frontal region, but from the area that will become the frontal region in the current frame, according to odometry. In order for both these regions to be scrolled off the screen, almost the entire image must be scrolled off-screen in either direction. This is an impossibility on our system, given its maximum turn rate of π radians per second.

2.3.4 Cross-validate matches

The change in yaw of an image patch from the previous frame to the current frame is that patch's estimate of the robot's rotation. To detect outliers, we cross-validate by having each patch "vote" for every other patch whose estimate differs by less than θ_p. Patches whose vote tally is more than half the number of patches are deemed reliable, while others are rejected as outliers. The rotation estimate shared by all inliers is taken as the robot's rotation between the previous and current frames. When using a small number of patches, a pair of frames may occasionally present no patches with a sufficient number of votes. On such frames we let the wheel odometer supply the change in pose.

2.3.5 Localizing the robot

The robot's current pose is estimated as:

$$p' \quad = \quad p + R_{\frac{\theta_v}{2}} R_{-\theta_w} \Delta p_w \tag{2.4}$$

Where p' and p are the current and previous pose estimates, Δp_w is the change in pose as reported by wheel odometry, θ_v and θ_w are the change in yaw as reported by visual odometry and wheel odometry, and R_θ is a rotation matrix representing a yaw rotation by θ. The concatenation $R_{\frac{\theta_v}{2}} R_{-\theta_w}$ expresses the fact that we undo the odometry-reported rotation θ_w and replace it with $\frac{\theta_v}{2}$. We use the midpoint method to numerically integrate the pose forward, hence the use of $\frac{\theta_v}{2}$ rather than θ_v.

In blending visual and non-visual odometry, we chose not to employ probabilistic model-based sensor fusion techniques, due to the highly non-Gaussian nature of wheel slip in outdoor terrain (see section 2.2.1). However it is simple enough to model the uncertainty of our bearing-only visual odometer, allowing for model-based sensor fusion with other sensors, or with wheel odometry in settings in which it is better behaved. In section 2.3.3, we described how we search for image patches by calculating its normalized cross-correlation within a search area, choosing the peak yaw θ_o as its matching location. We may locally fit a normal distribution $N(\theta_o, \sigma)$ to this peak, finding standard deviation σ by matching the second derivative of $N(\theta_o, \sigma)$ to the numerical second derivative of the cross correlation profile around the peak. The procedure may be repeated for all patches within our consensus set, and their individual uncertainties σ_i may be merged in the standard manner to yield the standard deviation of the bearing estimate: $\sigma_\theta = \left(\sum_i \sigma_{\theta i}^{-1}\right)^{-1}$.

2.4 Implementation

The system described in this paper has been deployed on the DARPA/NREC LAGR platform, an autonomous outdoor rover. The robot runs on two powered wheels and two passive casters, and takes input from wheel encoders, an IMU, and a GPS unit. In addition it takes visual input from two stereo camera pairs, pointing slightly to the left and to the right, with fields of view that overlap slightly around the frontal direction. The robot provides three user-accessible computers, one of which runs the VO system described in this paper. We have implemented all software components in Lush, an interpreted language with compilable functions. The visual odometer is entirely compiled, and runs on one of the camera computers. We captured the camera images at a low resolution of 160 x 120 pixels, and used six image patches of 13 x 3 pixels. The Intel Performance Primitives (IPP) library was used for the spherical image transform, Harris corner detection, and normalized cross-correlation. The hybrid VO system runs within the same thread as the short-range stereo-based obstacle detector [44], running at 6 Hz. The processor time is also shared by a long-range (5 to 150 meters) obstacle detector [18] running in a separate thread at 1 Hz. The "IMU + wheel" and "GPS + IMU + wheel" trajectories shown in figure 2.4 were calculated using tuned EKF pose estimators provided with the platform.

2.5 Results

The hybrid VO system has been tested on various types of outdoor terrain including the area around an office building, an open field, and a narrow path through a forest. For the results presented here, we recorded logs in these settings, and ran both our hybrid VO and the full 6-DOF VO of [1] on them, as a benchmark for accuracy and processor time. Figure 2.4 shows the pose trajectories of three runs. Predictably, wheel odometry fused with IMU consistently fares the worst.

The EKF fusion of wheel odometry, IMU, and GPS does better, except in the forest where the GPS signal can be both sporadic and inaccurate. Even with clear GPS reception, the GPS-aided trajectory suffers from discontinuities due to satellites coming in and out of reception. Full VO and hybrid VO perform comparably in all three runs, except for figure 2.4b, where a forward wheel slip was deliberately induced by running the robot up against a curb that was too high to surmount. All but the full visual odometer are fooled into believing that the robot made it over the curb. The plot in 2.4c shows the robot going down a narrow path through a forest. Accurate, high-frequency estimates of the robot bearing are particularly important in such settings, where false rotations due to wheel slip are frequent, and can cause a robot to counter-steer into entangling obstacles on each side. The hybrid VO retraces the path accurately after a quick 180-degree turn.

Figure 2.5 shows the drift from GPS (taken here to represent ground truth) over time for wheel odometry, hybrid VO, and pure VO. The data is from 10 randomly chosen runs, manually vetted for inaccurate GPS such as that of figure 2.4c.

The average CPU cost per frame of each of these runs is reported in table 2.1. The runtimes shown are those of a Pentium 4M laptop at 2 GHz, running off of image and sensor data logged by the robot. The robot's CPUs are approximately 2.5 times faster. While our system does not track translations, it does use range information to rule out features that are too close to the robot. As discussed in section 2.3.2, we get this information "for free" by appropriating the stereo image already calculated by our obstacle classification system. If no such stereo image data is available, we can also adopt the approach of [1], where a patch is searched for in the other stereo camera to estimate distance on a per-patch rather than per-pixel basis. In table 2.1, the runtimes for running just the hybrid VO, and for

Table 2.1: CPU time per frame on a 2 GHz Pentium 4M for full VO [1] and hybrid VO on the three courses shown in figure 2.4.

Log file	Full VO	Hybrid VO + range	Hybrid VO
Field Loop	266 ms	11.5 ms	8.0 ms
Building Lap	238 ms	11.0 ms	8.2 ms
Forest Path	153 ms	14.0 ms	9.3 ms

running the hybrid VO with per-patch stereo matching, are shown separately. The full VO runtime is best compared to the latter.

2.6 Conclusions and Future Work

We have presented an efficient hybrid wheel/visual odometer capable of localizing an autonomous robot in unstructured outdoor terrain at 5 to 10 percent of the computational cost of existing VO systems. Hybrid VO has the potential to enable accurate visual localization on platforms for which previous VO systems are prohibitively demanding. We have tested our system in outdoor terrain of varying visual complexity, including open fields with minimal visual features, and forest paths where GPS is error-prone and roots and leaves make wheel slip frequent.

We have demonstrated that faraway features can be used to estimate side-to-side rotation independently of the other degrees of freedom. As mentioned earlier, Kaess et. al. use a similar method, and follow up by estimating translation using nearby features. This is done to boost robustness to degenerate data [28]. We believe, however, that a similar approach can be taken with a different focus: to improve speed for 6-DOF VO, as we have done for 3-DOF VO.

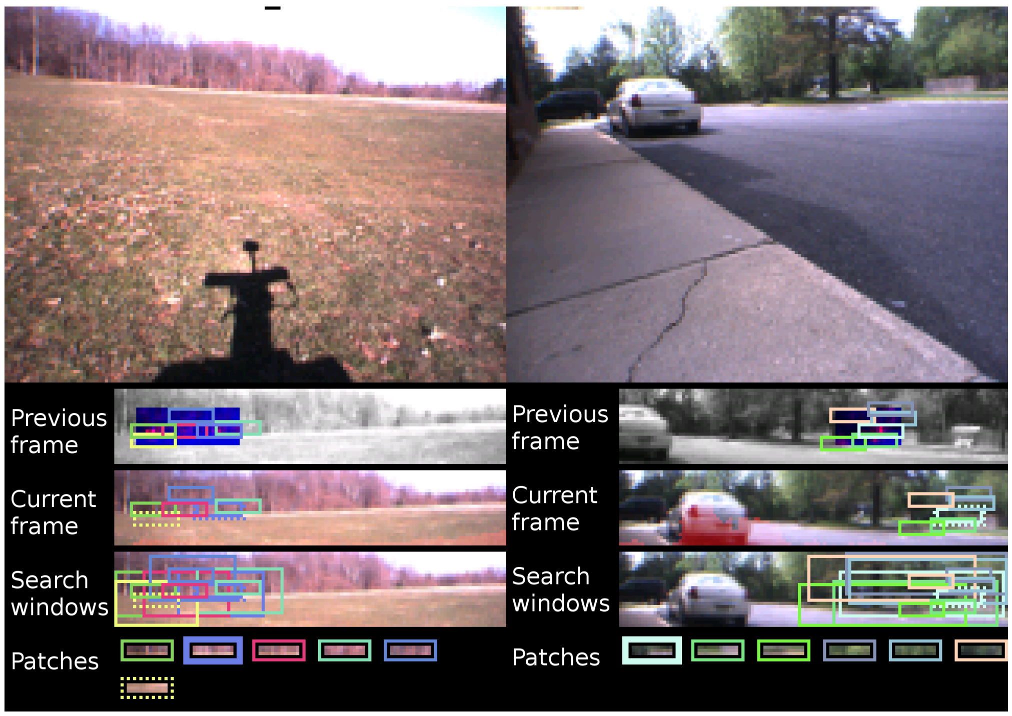

(a) Open field (b) Office parking lot

Figure 2.3: The robot's view, while running two of the courses in figure 2.4. "Previous frame" shows the spherically projected horizon image. Harris corners are detected in a region shown in blue, defined either as the frontal direction (figure 2.3a), or as what will become the frontal direction in the current frame, according to wheel odometry (figure 2.3b). Image patches are sampled around the strongest corners. "Current frame" shows their matches in the current frame. "Search windows" shows their search areas, defined to span the patch's position in the previous frame and its position in the current frame as predicted by wheel odometry. Figure 2.3b has wider search windows because the robot is in the middle of a sharp turn. "Patches" shows the isolated patches. The patch framed by yellow dots is a discarded outlier patch. Comparing the yellow rectangle in the previous and current frames, we can see that it has shifted by one pixel relative to the other patches.

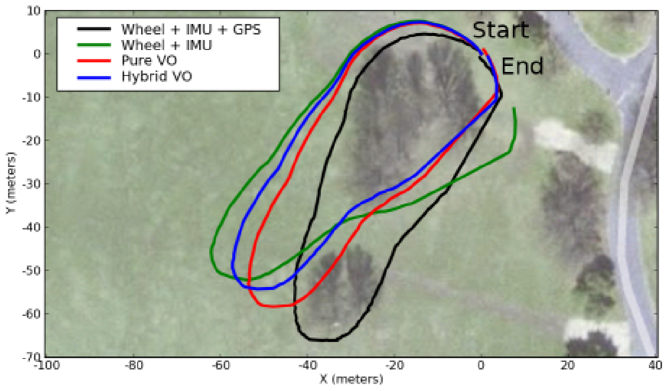

(a) Field Loop: A closed loop around two tree clusters.

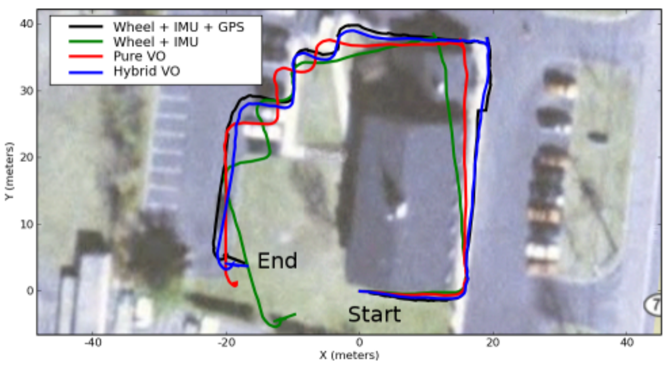

(b) Building Lap: A partial loop around a building.

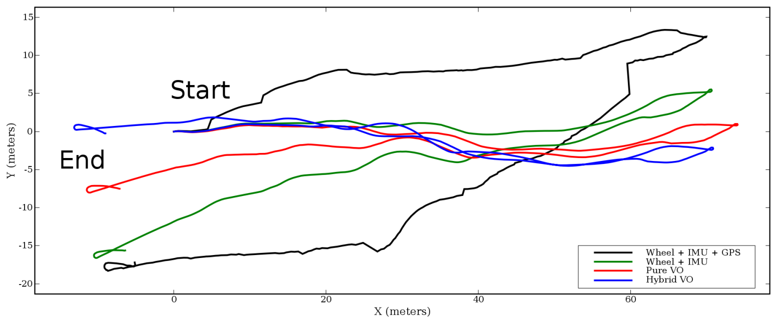

(c) Forest Path: Down a narrow forest path and back.

Figure 2.4: Vehicle trajectories, as measured using wheel odometry + IMU, wheel odometry + IMU + GPS, full VO [1], and vision-corrected wheel odometry. Non-GPS trajectories are aligned to the initial orientation estimate given by GPS, which can be noisy. In figure 2.4a, the robot's initial pose and final pose are identical. A trajectory's correctness may therefore be evaluated by the size of the opening in the loop. In figure 2.4b the robot follows the sidewalk between the robot's first turn and sixth turn. The sidewalk's shape serves as ground truth during this segment. In figure 2.4c, the robot traverses a narrow forest path, then backtracks down the same path. GPS is inaccurate and disruptive in wooded areas such as these.

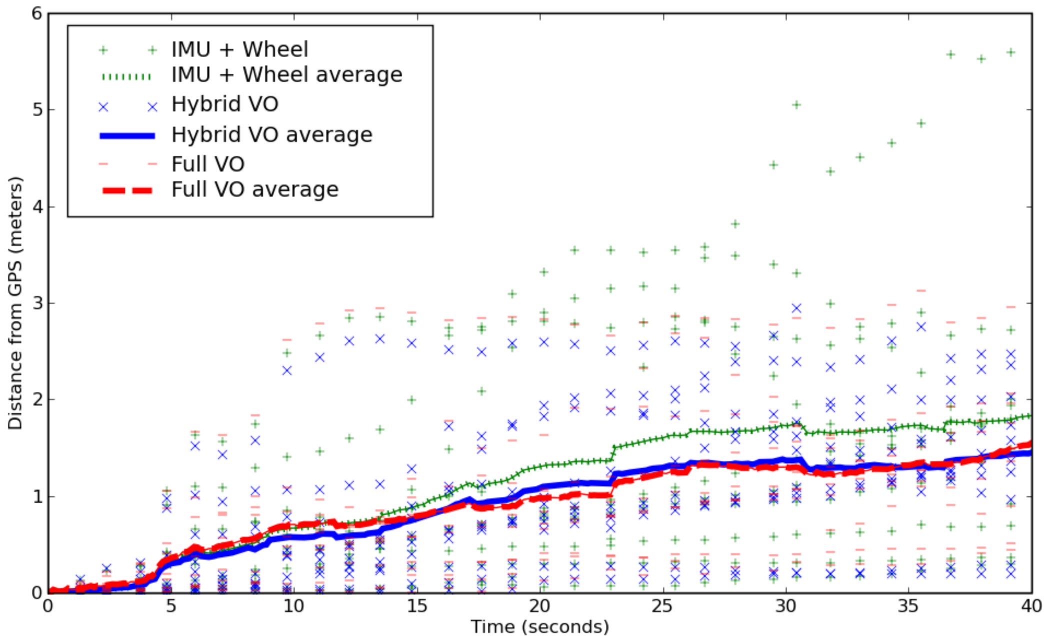

Figure 2.5: Drift from GPS position over time. The dots show the distances of estimated trajectories from the GPS position for 10 randomly chosen runs. The lines show the corresponding averages over all runs. The average distance traveled (as measured by GPS) was 30.3 meters.

3

Hybrid Hessians for SLAM with Tunable Cost and Accuracy

We present Hybrid Hessian Optimization ("H_2O"), an online 3D SLAM algorithm with flexible per-frame cost. Our main contribution is to allow the robot to choose how much computation to spend on SLAM in a given timestep. Set to maximum accuracy, our method gives the same result as exact solvers. Set to maximum speed, our method achieves linear-time speed, like fast stochastic solvers, while still maintaining better accuracy. How much computation should be spent on SLAM in a given frame? This decision belongs on the field, not in the design room. H_2O enables this flexibility.

In addition, H_2O combines strengths found individually in exact and stochastic solvers, but not together. Like exact methods, it can process GPS constraints without the pose staggering seen in stochastic solvers (the "dog-leg problem"). Like stochastic methods, it is robust against noisy input, which can trap exact methods in local minima.

We present results from the Google Street View database, and compare our method with results from TORO, one of the fastest stochastic solvers. We show that our solver is able to achieve higher accuracy while operating within real-time bounds. The open-source code is available online at `http://mkg.cc`.

3.1 Introduction

Simultaneous localization and mapping, or SLAM, is a critical prerequisite to autonomous mobile operation. Put differently, SLAM typically serves as a foundation for higher-level tasks, rather than itself being the raison d'être of a robot. It is therefore important that the SLAM cost be controllable, to accommodate unpredictable CPU demands made by other components in the field.

A common solution is to run SLAM in a separate thread, which can be deprioritized as necessary. There are a number of drawbacks with this approach. For one, this may delay the closing of newly discovered loops, exactly at the moment when this loop-closure is most needed. For example, making the correct turn at an intersection may depend on solving the loop-closure introduced by that very intersection. Furthermore, running SLAM in a separate thread prevents it from directly providing the current pose estimate. This necessitates a separate local odometry system for this task, increasing system complexity. Finally, delaying a loop closure caused by one landmark can cause subsequent landmark associations to suffer, due to uncorrected drift.

We present a method that allows the user to specify the amount of CPU time to use in a given SLAM update, where more time yields more accuracy. This allows our SLAM algorithm to stay within the control loop, providing the most recent pose estimate directly to the rest of the system without need of thread synchronization or odometry subsystems. It processes simple odometry-based updates in the expected $O(1)$ time, while loop closures cost $O(N)$ to $O(N^2)$ time in the size of the loop.

This controllable cost is the salient feature of H_2O. However, H_2O also combines several strengths seen individually in other SLAM algorithms, but not together. From stochastic methods, it inherits a robustness to sensor noise and poor initial poses, along with quick, real-time closure of large loops in (if so chosen) $O(N)$ time. From exact methods, it inherits smooth loop closures without "dog-leg" discontinuities, and the ability to process position-only or orientation-only constraints such as GPS or compass input.

We demonstrate the above features on both commonly used datasets and real-world urban data taken from the Google Street View database. The source code is available online at `http://mkg.cc`.

3.2 Related Work

Early filter-based SLAM algorithms, such as EKF SLAM, incorporated new observations into an Extended Kalman Filter (EKF) [46], at a cost of $O(N^3)$ in the size of the map. Updates start to fall below real-time performance with as few as 200 landmarks, which for visual SLAM can amount to a handful of rooms [9]. Performance can be improved by selective sparsification of the information matrix, [47, 50], but reconstructing the map from this matrix remains costly.

A more recent improvement is the "pose graph" formulation of SLAM, which represents robot and landmark poses as nodes, constrained to each other by spring-like edges, representing observations. Relaxing this node-spring graph yields the least-squares optimal estimate of all poses given all observations. Doing so naively with dense Gauss-Newton minimization costs $O(N^3)$ in the number of nodes, but by exploiting the sparsity of the graph, typical SLAM methods do far better. The many methods using this representation can be roughly divided into "exact" and "stochastic" methods.

In machine learning, stochastic optimization is often preferred over exact optimization for its fast convergence and robustness to local minima [5, 32]. From stochastic optimization, SLAM methods such as SGD and TORO [17, 37] borrow the idea of relaxing one constraint at a time. This results in fast-converging updates whose very inexactness helps to escape from local minima that would trap an exact solver [38]. Such local minima are a risk when the initial pose estimate is far from the global minimum due to noisy sensors such as GPS. H_2O is similarly capable of recovering solutions from poor initial estimates by noisy sensors.

Unfortunately, both SGD and TORO get their speed by neglecting off-diagonal terms in the information matrix. This de-correlates position and rotation variables,

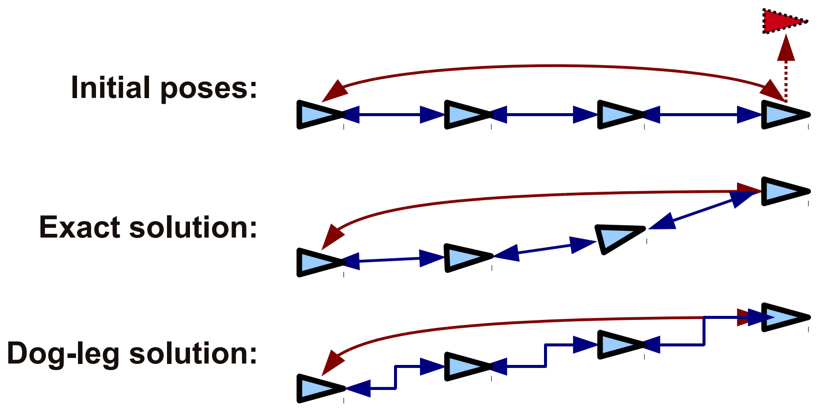

Figure 3.1: **The dog-leg problem** occurs when an error in position is corrected by position updates only, without also updating rotations. Here we see a relaxation of the red constraint, with and without the dog-leg problem.

leading to the distortion known as the “dog-leg problem”. This problem becomes particularly noticeable when closing long loops, such as those typical of outdoor urban exploration around large city blocks 3.8e. It also prevents these methods from using GPS at all, since position errors would be corrected by position updates only, without also adjusting rotations (fig. 3.1). H_2O does not suffer from this problem.

Pose graphs are sparse, and can be efficiently relaxed using techniques from sparse linear algebra. Methods like iSAM2 [27] find the exact solution given a sufficiently good initial estimate. Instead of recomputing the solution for every update, new observations are processed incrementally at much reduced cost. Drawbacks include the risk of falling into local minima, and the high cost of closing large loops. For planar graphs, N-pose loops cost only $O(N^{1.5})$, but in the non-planar case (as is common in 3D), the loop can cost up to $O(N^3)$. The robot must therefore be prepared to handle load spikes from the SLAM system when closing large loops, and work around them either by deferring the loop-closure, or deferring tasks that depend on it.

Some authors have worked around this cost by limiting the scope of SLAM to a local region around the robot. Bibby et al do this to gain a measure of robustness to moving features [4]. Sibley performs local relaxation with similar goals to ours: to maintain real-time performance [45]. While this does boost speed, it is not without drawbacks. Faraway landmarks, if they are retained at all, can drift, making it difficult to detect them for loop-closure once the robot returns to them. Also, keeping the map in a single consistent coordinate frame can help with collaborative mapping, or alignment with prior surveying, such as aerial imagery or GIS. Finally, if a loop size exceeds the local relaxation bounds, these methods must choose between closing the loop (at full cost) or leaving a discontinuity in the loop. For these reasons, we have chosen to focus on real-time, globally consistent SLAM.

The HOG-MAN algorithm [16] also performs local SLAM, but maintains global consistency by connecting a simplified, easy-to-solve pose graph to the real pose graph. The simple graph can be solved quickly, maintaining global consistency, while local SLAM is performed on local regions of the full-resolution graph. The cost of closing a loop remains unmitigated, however, costing up to $O(N^3)$ in the size of the loop.

In [10], Dellaert et al propose a two-pass solution, in which a sparse linear solver first relaxes only the "local" edges. The result is used to precondition a conjugate-gradient step to relax the non-local "loop" edges. H_2O also uses a preconditioner to regularize the relaxation of expensive edges. However, these edges are typically relaxed one at a time, enabling online operation.

3.3 Algorithm

In this section, we first review background on the pose graph SLAM representation, our hierarchical parametrization, and linearized SLAM updates. We then introduce H_2O in terms of this background, starting with the most common case of relaxing one edge at a time. We then generalize to relaxing any arbitrary set of edges and nodes, while maintaining global consistency for the rest of the map. Finally, we demonstrate dynamic reparametrization, and its importance to guaranteeing real-time performance on all frames.

3.3.1 Pose Graphs

This work concerns itself with the pose graph formulation of SLAM. A pose graph is formed of nodes, representing poses, and edges, which connect two poses, and represent a sensor reading of their relative pose. For example, an odometer may measure the relative transform from the previous pose a to the current pose b to be transform k. We connect poses a and b by an edge representing this reading. This edge defines an energy function that penalizes deviations of the relative pose $p = a^{-1}b$ from its measured value k:

$$E = (k - p)^T S(k - p) \tag{3.1}$$

Here S is the inverse covariance of the odometry sensor, so labeled because it represents the "stiffness" of the spring-like edge connecting a and b.

Note that poses may represent current and prior robot poses, and poses of any landmarks being tracked. Edges are sensor-agnostic. Their relative pose estimates may come from laser scan-matching, IMU, visual odometry, etc. Global

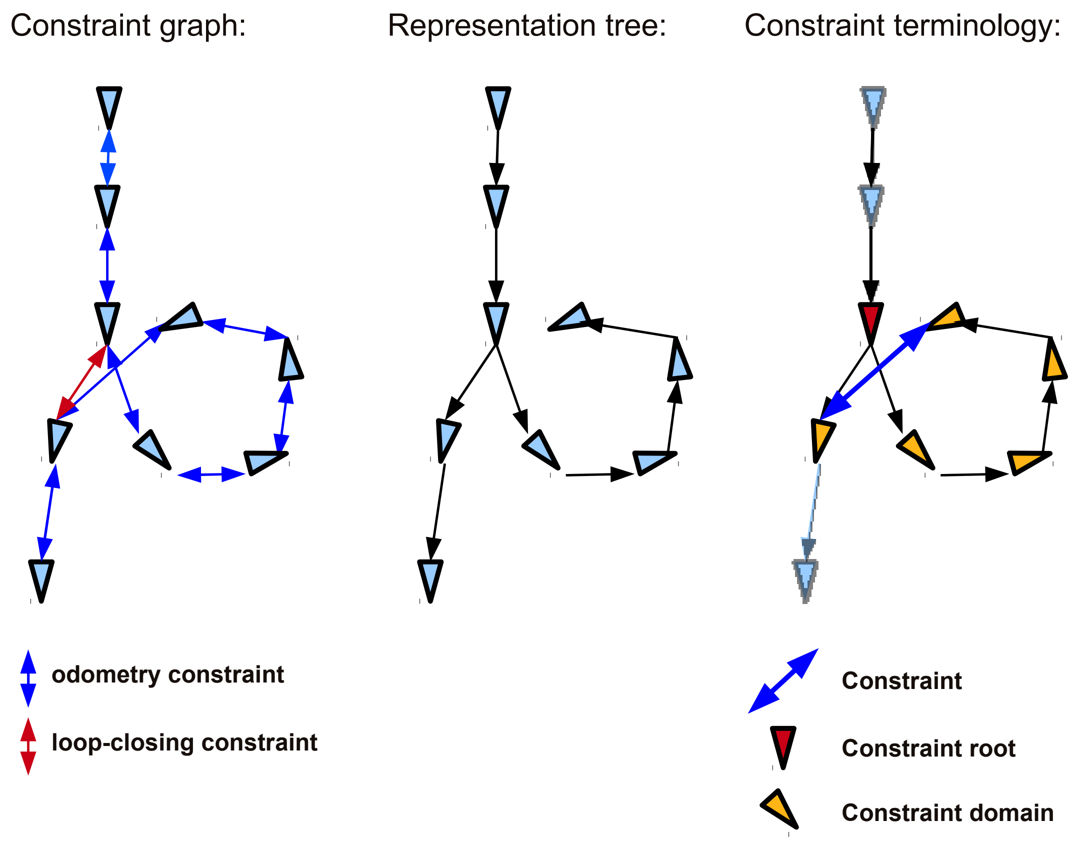

Figure 3.2: **Pose tree terminology** The image on the left shows a small pose graph, with odometry edges in blue, and a loop-closing edge in red. We use a hierarchical pose representation, defining each pose relative to its parent in a spanning tree. Such a tree is shown in the center. The right figure introduces some terminology: A constraint's domain is the set of poses whose values affect the constraint energy. The constraint's root is the topmost node in the path from one node of the constraint to the other. It is not part of the constraint domain.

sensors such as GPS and compasses are no exception: they constrain the relative position/rotation between the earth node (a landmark of sorts) and a robot pose.

SLAM thus reduces to a nonlinear minimization problem: we wish to find the values of a, b, and all other poses, which give the global minimum of the sum of edge energies. When edge energies are interpreted as log-probabilities, this yields the maximum a posteriori estimate of all poses given all sensor inputs.

3.3.2 Pose Trees

Like [17], we use a spanning tree of the pose graph to define a hierarchical parametrization, where we define each pose in coordinates relative to its parent in the tree. Fig. 3.2 shows a pose graph, and one possible pose tree that spans it. We now introduce some terminology. The "path" of the edge is the set of nodes on the path through the tree from a to b. The "root" of the edge is the node in this path with the smallest tree depth. This node does not affect a and b's relative pose p, since translating or rotating the root merely translates or rotates its entire subtree together. All other nodes on the path do affect p and the edge energy (3.1), and for this reason, we call them the edge's "domain". When SLAM relaxes an edge to a lower energy, only its domain nodes are moved.

We can accommodate GPS, compass, and other global-coordinate sensors by placing at the root of the tree a node representing the earth. For example, a GPS reading on node a is an edge between the earth node and a, constraining their relative position. Because the earth is at the root of the tree, it is outside of any edge's domain, and is therefore left unchanged by SLAM, as is appropriate.

3.3.3 Linearized updates

We represent our poses as 7-dimensional vectors composed of a position vector and quaternion (quaternions are re-normalized after each update). We collect all poses in a single vector z. For a constraint c connecting poses a and b, Let $f_c(z)$ be the relative pose between a and b. Rewriting p in (3.1) as $f_c(z)$, we get this expression for edge energy E_c:

$$E_c(z) = (f_c(z) - k_c)^T S_c(f_c(z) - k_c) \tag{3.2}$$

In EKF terminology, f_c is the prediction function, k_c is the "observation", and S_c is the inverse of the sensor covariance matrix.

We may use Cholesky factorization to split S_c into $S_c = L_c L_c^T$. We then define the edge residual r_c as:

$$r_c(z) = L_c^T(f_c(z) - k_c) \tag{3.3}$$

Plugging (3.3) into (3.2) we get a simpler form:

$$E_c = r_c^T r_c \tag{3.4}$$

The edge Jacobian J_c is the derivative of $r_c(z)$, evaluated at the current value $z = \bar{z}$:

$$\begin{aligned} J_c &= \left.\frac{\partial r_c}{\partial z}\right|_{\bar{z}} && (3.5) \\ &= \left.\left[\begin{array}{cccc} \frac{\partial r_c}{\partial z_1} & \frac{\partial r_c}{\partial z_2} & \cdots & \frac{\partial r_c}{\partial z_N} \end{array} \right]\right|_{\bar{z}} && (3.6) \end{aligned}$$

The Jacobian above is a row of 7×7 blocks of the form $\frac{\partial r_c}{\partial z_i}$, where z_i is the i'th pose. Because r_c only depends on those poses in edge c's domain, blocks corresponding to other poses are all zero, making J sparse.

Stacking the Jacobians and the residuals of all M edges, we get the total Jacobian J and total residual r:

$$J = \begin{bmatrix} J_1 \\ \vdots \\ J_M \end{bmatrix} \quad (3.7) \qquad r = \begin{bmatrix} r_1 \\ \vdots \\ r_M \end{bmatrix} \quad (3.8)$$

The total energy E is the sum of edge energies E_c:

$$\begin{aligned} E &= \sum_c E_c && && (3.9) \\ &= \sum_c r_c^T r_c && \text{from (3.4)} && (3.10) \\ &= \|r\|^2 && \text{from (3.8)} && (3.11) \end{aligned}$$

To minimize E, we start by linearizing it around $\bar{z}$:

$$E \approx \|r(\bar{z}) + Jx\|^2 \qquad (3.12)$$

We seek a perturbation x to poses z that will minimize E.

Differentiating (3.12) with respect to x and setting it to zero, we arrive at the normal equations of the Gauss-Newton method:

$$2J^T(Jx + r) = 0 \qquad (3.13)$$

$$Hx = -J^T r, \qquad (3.14)$$

Here H is $J^T J$, also known as the approximated Hessian or the information matrix. Equation 3.14 may be upper-triangularized by the Cholesky decomposition

$H = R^T R$, followed by one back-substitution:

$$R^T R x = -J^T r \tag{3.15}$$

$$Rx = b \qquad \text{(back-substituted } R^T\text{)} \tag{3.16}$$

Back-substituting R then solves for x.

We can also arrive at 3.16 by another route, by setting $Jx + r = \vec{0}$ and QR-factorizing J:

$$Jx = -r \tag{3.17}$$

$$QRx = -r \tag{3.18}$$

$$Rx = -Q^T r \tag{3.19}$$

$$Rx = b \tag{3.20}$$

This is the approach taken by Dellaert and Kaess in $\sqrt{SAM}$ [11]. We note that when J is nearly upper-triangular, this QR-factorization can take $O(N^2)$ time, as opposed to the $O(N^3)$ taken to Cholesky-factorize the normal equations. We will exploit this fact in section 3.3.5 to efficiently solve for stochastic updates.

Having solved for update x, we add it to pose parameters z:

$$z \leftarrow z + x \tag{3.21}$$

This is followed by normalizing the quaternions in z.

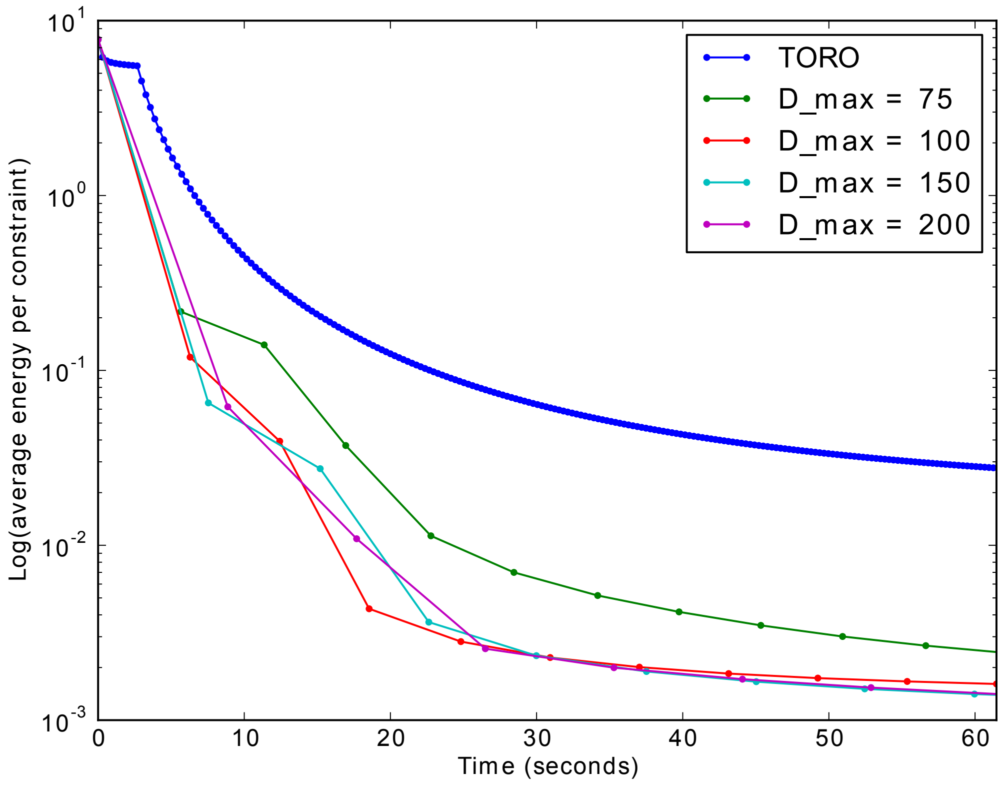

Figure 3.3: χ^2 **error vs time, Valencia dataset** The average constraint energy vs time (in seconds) for TORO [17] and our method. For our method, we use different values for the maximum limit D_{max} on the number of poses solved per constraint, as described in section 3.3.6.

3.3.4 Stochastic Updates

The update x described above is expensive to evaluate, since it is calculated using all edges in the graph. An alternative is to inexpensively calculate one approximate update x_c from each edge c. Such "stochastic" updates have a long history in machine learning [5, 32], as they converge much more quickly than exact updates, and provide some robustness to local minima [22, 39]. The robustness arises from the fact that stochastic optimizers experience some "jitter" in their trajectory towards the local minimum, which can help escape shallow local minima. Oscillations due to the inexactness of these updates are mitigated by using a decaying learning rate, as will be discussed in section 3.3.11. In this section we derive our expression for x_c.

Plugging (3.7) and (3.8) into the right-hand-side of (3.14) gets:

$$Hx = -\sum_c J_c^T r_c \tag{3.22}$$

This lets us express the total update x as a sum $x = \sum_c x_c$ of constraint-specific updates x_c, where:

$$x_c = -H^{-1} J_c^T r_c \tag{3.23}$$

In practice, we compute x_c by solving the linear system:

$$Hx_c = -J_c^T r_c \tag{3.24}$$

In stochastic relaxation, the parameters z are updated by one x_c at a time, rather than by their sum, x. In many applications, this converges quicker, and typically computation is saved by not recalculating $H = \sum_c J_c^T J_c$ from scratch after each constraint update.

Our goal is to speed up solving for x_c and make it real-time. One could use an approach similar to second-order back-propagation in neural networks [32], where H is reduced to a diagonal by zeroing all off-diagonal elements. Unfortunately, while this does reduce the cost to linear-time, it also prevents convergence in the case of SLAM. The reason is that zeroing the off-diagonals greatly reduces the matrix norm $\|H\|$, making the resulting update x_c very large. Large updates to the poses, particularly to the rotations, can easily prevent convergence, since rotating a node rotates its entire sub-tree. In [38], Olson prevents this by using an approximation to J_c where each nonzero block is replaced by a constant diagonal matrix. This eliminates any large derivatives it may contain, and removes the need to calculate derivatives. While the resulting algorithm is very fast, it erases the correlation between rotation parameters and position residuals, causing the "dog-leg problem". TORO [17] employs a similar simplification in 3D, with the same problem.

3.3.5 Hybrid Hessians

We now describe our approximation to H, which is easy to invert, avoids the dog-leg problem, and does not produce overly large updates.

We approximate H in (3.24) with a "hybrid Hessian" H_c specific to edge c. To construct H_c, we start by separating the full hessian $H = \sum_e J_e^T J_e$ into two terms, one containing the contribution of edge c, and another containing the contributions of all other edges, which we will call H_o:

$$H = J_c^T J_c + \sum_{i \neq c} J_i^T J_i \tag{3.25}$$

$$= J_c^T J_c + H_o \tag{3.26}$$

Recall that J_c is a row of N blocks (3.6), which makes H_o an $N \times N$ grid of blocks. Let $\mathfrak{B}$ be an operator which zeros all off-diagonal blocks. (In practice, we leave these blocks uncalculated.) We use it to construct H_c:

$$H_c = J_c^T J_c + \mathfrak{B}(H_o) \tag{3.27}$$

$$= J_c^T J_c + B_c \tag{3.28}$$

In other words, H_c is constructed from the full contribution of J_c, and the approximated contribution of all other edges B_c.

We obtain our stochastic update x_c by replacing H in (3.24) with H_c, and solving for x_c:

$$(J_c^T J_c + B_c)x_c = J_c^T r_c \tag{3.29}$$

This yields a solution to the following least-squares problem:

$$\min_{x_c} \left(\|J_c x_c - r_c\|^2 + \|\Gamma_c x_c\|^2 \right) \tag{3.30}$$

where Γ_c is the block-diagonal upper triangle of the Cholesky factorization:

$$B_c = \Gamma_c^T \Gamma_c \tag{3.31}$$

Without $\|\Gamma_c x_c\|^2$, (3.30) would be an under-constrained minimization problem for a single constraint c. We have regularized it using the block-diagonals of the full hessian, both to make it solvable, and also to prevent each update x_c from simply satisfying constraint c without regard to all other edges.

Before moving onto the next edge e, we can inexpensively calculate its regularizer B_e as:

$$B_e = B_c + \mathfrak{B}(J_c^T J_c - J_e^T J_e) \tag{3.32}$$

Again, the off-diagonal blocks are left uncalculated, making this a fast, linear-time operation in the number of nonzero blocks in J_c, J_e.

We recall that only the poses in constraint c's domain $\mathcal{D}_c$ affect c's energy, as seen in fig. 3.2. We can therefore solve a reduced-dimension version of (3.29) by omitting all rows and columns that do not correspond to poses in $\mathcal{D}_c$. We denote this omission using hats ($\hat{}$), as in:

$$(\hat{J}_c^T \hat{J}_c + \hat{B}_c)\hat{x}_c = \hat{J}_c^T r_c \tag{3.33}$$

One could solve this dense normal equation using Cholesky factorization. But since this is cubic in the size of $\mathcal{D}_c$, it may be unacceptably expensive for edges with large paths. Instead, as we did in (3.17) to (3.20), we will perform QR decomposition on the square-root information matrix form of (3.33):

$$\begin{bmatrix} \hat{J}_c \\ \hat{\Gamma}_c \end{bmatrix} \hat{x}_c = \begin{bmatrix} r_c \\ \vec{0} \end{bmatrix} \tag{3.34}$$

Note that left-multiplying both sides of (3.34) by $[\ \hat{J}_c^T \quad \hat{\Gamma}_c^T\ ]$ recovers (3.33). Equation 3.34 is a Tikhonov regularization of the under-constrained problem $\hat{J}_c\hat{x}_c - \hat{r}_c = 0$, with the Tikhonov matrix $\hat{\Gamma}_c$ constructed from diagonal blocks of the hessian H.

Now we write (3.34) block-by-block, showing only the nonzero blocks. Here,

J_c^i is the i'th block of $\hat{J}_c$, and Γ_c^i is the i'th block of the block-diagonal matrix $\hat{\Gamma}_c$, and d is the size of domain $\mathcal{D}_c$:

$$\begin{bmatrix} J_c^1 & J_c^2 & J_c^3 & \dots & J_c^d \\ \Gamma_c^1 & & & & \\ & \Gamma_c^2 & & & \\ & & \Gamma_c^3 & & \\ & & & \ddots & \\ & & & & \Gamma_c^d \end{bmatrix} \hat{x}_c = \begin{bmatrix} r_c \\ 0 \\ 0 \\ 0 \\ \vdots \\ 0 \end{bmatrix} \tag{3.35}$$

Equation 3.35 is nearly upper-triangular, with no element more than one block (7 spaces) below the diagonal. This allows us to fully upper-triangularize it (using Givens rotations) in $O(d^2)$ time, not the usual $O(d^3)$ for dense matrices. The subsequent back-substitution to solve for x takes $O(d^2)$ time as well. Updating B_c is $O(d)$ (3.32). The total cost of relaxing a constraint is therefore $O(d^2)$.

The longest possible path length is proportional to the depth of the tree, which in a balanced tree is $O(log(N))$ in the total number of poses. The expected running time for a single iteration through all M edges is therefore $O(Mlog(N)^2)$. In the next section, we show how this can be further improved.

3.3.6 Interpolated solving

In large pose trees with low branching factor (such as urban pose trees), the path length for some constraints can get into the thousands, making even $O(d^2)$ too costly for real-time operation on a single processor. Fortunately, it is possible to solve for an approximation to x_c within a user-chosen computational cost budget, ranging from $O(d)$ to $O(d^2)$. We do this by solving for a subset $\mathcal{S}_c$ of the nodes in the path $\mathcal{D}_c$, then distributing these updates over the remaining nodes.

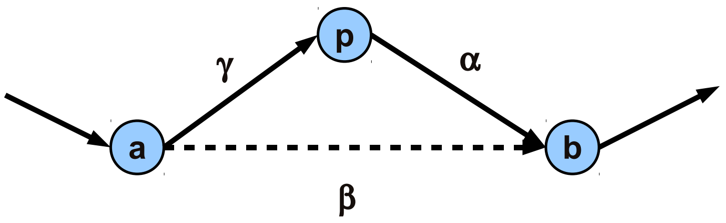

Figure 3.4: **Subsampling a constraint path** Subsampling a path by omitting node p, parent of b. Node b is now acted on by a temporary constraint β instead of α. The block corresponding to node b in the block-diagonal hessian approximation B must be updated accordingly, using equation 3.36. Constraint β is constructed from constraints γ and α.

3.3.6.1 Merging constraints

in (3.33), we solved for only the nodes in $\mathcal{D}_c$ by omitting from (3.29) the rows and columns corresponding to other nodes. We take the same approach here, solving for only the nodes in $\mathcal{S}_c \in \mathcal{D}_c$ by omitting other nodes' rows and columns in (3.33).

When omitting nodes from the path, we are replacing chains of constraints with single constraints, as shown in fig. 3.4. This is similar to the subgraph simplification of nested dissection [14]. This change affects the regularizer B_c (3.28), which must be updated accordingly.

Consider a pair of nodes a and b in $\mathcal{S}_c$, where a is b's closest ancestor in $\mathcal{S}_c$, or the edge root, whichever comes first (fig. 3.4). We replace a chain of constraints between a and b by a single constraint β. Let α be b's current parent constraint in the path. We update regularizer B as follows:

$$\tilde{B} = B - J_\alpha^T J_\alpha + J_\beta^T J_\beta \tag{3.36}$$

Note that (3.36) makes no mention of the omitted constraint γ. This is because γ only affects node p, which we are omitting anyway. Eq. (3.36) need only concern itself with the parent-edges of nodes in our selected subset $\mathcal{S}_c$. Both α and its replacement β are tree edges, so they have domain sizes of 1. Therefore, their Jacobians have one nonzero block each, making the update in (3.36) an $O(1)$ operation. Updating B is therefore $O(N)$ in the size of $\mathcal{S}_c$.

To calculate the J_β of merged edge β, we need its stiffness S_β and desired relative pose k_β (3.2). If $c_1 \ldots c_n$ are the edges merged to create β, we get k_β by taking the product of the desired transforms of $c_1 \ldots c_n$:

$$k_\beta = \prod_{i=1}^{n} k_i \tag{3.37}$$

Since stiffness is the inverse of sensor covariance, we find the merged stiffness S_β by applying the covariance merging rule $C_{merged} = \left(\sum_i C_i^{-1}\right)^{-1}$. In terms of stiffnesses this becomes:

$$S_\beta = \sum_{i=1}^{n} R_{ai} S_i R_{ai}^T \tag{3.38}$$

where S_i is the stiffness of c_i and R_{ai} is the desired rotation from node a to i.

In our experiments, we have taken the simple approach of omitting nodes evenly along the path. It is probable that more sophisticated and effective approaches exist. Possible examples include omitting more nodes further away from the edge

Table 3.1: Minimum values of D_{max} needed for convergence.

Dataset	nodes	edges	loop edges	max d	D_{max}
"Manhattan world"	3500	5598	2099	184	30
Valencia w/o GPS	15031	15153	122	1161	40
Valencia w/GPS	15031	15440	409	1834	90
Paris1 w/o GPS	27093	27716	590	3599	190
Paris1 w/GPS	27093	28943	1817	3605	200
Paris2 w/o GPS	41957	55392	13384	701	150
Paris2 w/GPS	41957	56109	13878	802	200

being relaxed, or more densely sampling nodes around areas of the path with high curvature.

3.3.6.2 Solving and distributing the update

After modifying B with (3.36) and eliminating the omitted nodes' rows and columns from (3.34), we get the reduced orthogonal decomposition:

$$\begin{bmatrix} \tilde{J}_c \\ \tilde{\Gamma}_c \end{bmatrix} \tilde{x}_c = \begin{bmatrix} r_c \\ \vec{0} \end{bmatrix} \tag{3.39}$$

This is exactly analogous to (3.34), except only the rows and columns corresponding to nodes in $\mathcal{S}_c$ are retained. Also, $\tilde{\Gamma}_c$ is formed by the Cholesky decomposition of the updated regularizer $\tilde{B}_c$ from (3.36). After solving for $\tilde{x}_c$, we revert the modified blocks of B to their previous values before updating by (3.32).

If we apply the subsampled update $\tilde{x}_c$ directly to z, the path will bend only at $\mathcal{S}_c$'s nodes in c's path, making the path discontinuous. Instead, we use the method used by TORO to distribute a pose adjustment over a path. In our case, the desired pose adjustment is given by temporarily applying $\tilde{x}_c$ to z and normalizing the affected quaternions. The desired pose adjustment is the transform from b's old pose to its new pose. We then distribute this adjustment over the nodes from a down to b, not including a. As in TORO, we use the diagonal elements of B as the distribution weights. For details on this distribution algorithm, we refer the reader to [17]. This does not cause dog-legs, because $\tilde{x}_c$ updates rotations even for position-only constraints.

3.3.7 Batch solving

It is possible to build a hybrid hessian $H_\mathcal{C}$ for updating a set $\mathcal{C}$ of constraints at once, by including the off-diagonal blocks of multiple constraints' $J_c^T J_c$.

$$H_\mathcal{C} = \sum_{c \in \mathcal{C}} J_c^T J_c + B_\mathcal{C} \tag{3.40}$$

Here the block-diagonal regularizer $B_\mathcal{C}$ is formed from all edges not in $\mathcal{C}$:

$$B_\mathcal{C} = \sum_{i \notin \mathcal{C}} \mathfrak{B}(J_i^T J_i) \tag{3.41}$$

The equations to QR-factorize are then:

$$\begin{bmatrix} J_\mathcal{C} \\ \Gamma_\mathcal{C} \end{bmatrix} x_c = \begin{bmatrix} r_\mathcal{C} \\ \vec{0} \end{bmatrix} \tag{3.42}$$

Here $\Gamma_\mathcal{C}$ is created as before by the Cholesky decomposition $B_\mathcal{C} = \Gamma_\mathcal{C}^T \Gamma_\mathcal{C}$. We form the batch-Jacobian $J_\mathcal{C}$ and batch-residual $r_\mathcal{C}$ by stacking the Jacobians and residuals for edges in $\mathcal{C}$, much as we did in (3.7) and (3.8).

We vertically stack J_c and r_c corresponding to the constraints c in $\mathcal{C}$ to get $J_\mathcal{C}$ and $r_\mathcal{C}$. When $\mathcal{C}$ contains all the constraints in the posegraph, $J_\mathcal{C}$ becomes J, and

$\Gamma_{\mathcal{C}}$ vanishes, since there are no edges that are not in $\mathcal{C}$ (3.41). This reduces (3.42) to the full exact update equation (3.17), yielding the exact update when solved.

3.3.8 Node and edge reordering

As pointed out by several authors [11, 27], the cost of solving for a batch-update like x_c depends greatly on the row and column ordering used in (3.42). In offline $\sqrt{SAM}$ [11] and SPA [31], this is done using approximate minimum degree (AMD), a heuristic devised for general sparse problems [7]. Much work has been done in finding good orderings for sparse QR factorizations, e.g. [20].

Unlike these methods, we usually solve for one edge at a time, resulting in a matrix that is already so close to upper-triangular (3.35) that reordering its columns will not improve efficiency. When we do batch-relax multiple edges, we do so with a handful of GPS edges, for reasons described in section 3.3.10. GPS edges have long paths that reach from the constrained node all the way up to the Earth node at the root of tree. This leads to dense rows, which can limit the usefulness of AMD [2]. We therefore use a simple, alternative approach that has sufficed for our needs of relaxing a handful of constraints within real-time bounds.

The cost of upper-triangularizing the left-hand side of (3.42) increases sharply with the number of sub-diagonal nonzeros. We therefore seek to permute the rows and columns in a manner that keeps most nonzeros above the diagonal.

To illustrate, we show the extreme case of batching all edges together, i.e. solving for the exact solution. Fig. 3.5 shows the block-sparsity pattern of the total Jacobian J (3.7), constructed from all edges in Olson's Manhattan dataset. Each row is an edge Jacobian J_e (3.6). Before reordering, these are stacked in chronological order of their corresponding edges. Each column corresponds to a node, again listed in chronological order of their nodes. We will first reorder the nodes (columns), then the edges (rows). To do so, we first introduce some terminology.

A node's "edge count" is the number of edges whose Jacobians are affected by that node. We may determine a node's edge count by counting the number of nonzero blocks in its corresponding column in $J_{\mathcal{C}}$. A "segment" is a chain of nodes up the tree from child to parent. It starts from a branching node in the tree, and stops just below the next branching node. All the nodes in a segment affect the same set of edges, and therefore have the same edge count. We arbitrarily assign unique ID numbers to each segment.

We sort the nodes (columns) primarily by increasing edge count, breaking ties by segment ID, then by depth. By doing so, the columns (nodes) that affect the same rows (edges) are grouped together, and columns that affect the most edges are placed to the right of the matrix. This ordering is evident in fig. 3.5b, where the densest columns can be seen grouped to the right.

Having sorted the columns, we now sort the edges by the index of the first nonzero. This moves many of the nonzeros out of the lower triangle, leading to a "semi-triangular" shape that is easier to upper-triangularize.

It is important to note that our method focuses on stochastic optimization, with exact solving offered as an option to be used infrequently. Exact updates with our method cost more than when performed using solvers designed for exact updates only, such as iSAM [27]. This is because we use hierarchical poses, which produce denser J matrices when all edges are batched together.

3.3.9 Online Tree Balancing

The worst-case cost of a new edge is $O(d_t^2)$, where d_t is the maximum depth in the tree. This happens when the new edge connects the deepest node in the tree to another node, and their common ancestor is the root. To minimize this worst-case cost, we must keep the tree depth d_t small by maintaining a balanced pose tree. In this section we describe our method for doing so.

Let e be a new edge connecting nodes a and b, with tree depths d_a and d_b. If d_b is greater than d_a+1, we may reduce it to d_a+1 by making a the new parent of b. Having reduced b's depth, we must then recursively check its neighbors in the pose graph to see if we may reduce their depths as well, by making b their parent. This recursive tree restructuring can be done by performing a breadth-first traversal of the graph from b, halting the recursion if no neighbor of the current node benefits from becoming its child.

When an edge connects two separate pose graphs, their trees must be merged. We do this by simply growing the larger graph's spanning tree into the smaller graph, using a breadth-first traversal starting from the connecting node.

When we give a node a new parent, this changes the path up the tree from that node. This changes the domain of any edge whose domain contains that node. For any such edge e, we must update its contribution $J_e^T J_e$ to regularizer $B = \sum_i \mathfrak{B}(J_i^T J_i)$. This is a linear-time operation in the combined size of e's old and new domains.

By maintaining a balanced tree, we limit the tree depth to $d_t = O(log_b(N))$, where b is the branching factor of the spanning tree. The worst case cost C_{max} is then $C_{max} = O(log_b^2(N))$. As shown in section 3.3.6, interpolated solving can further reduce this cost to being linear in the tree depth, giving a minimum bound

Algorithm 1 H_2O

```
loop
    Receive new edge $e$ from sensors.
    AddEdge($e$)    // See algorithm 2
    if $e$ is a GPS edge then
        $\mathcal{G} \leftarrow$ GetUpstreamGPSes($b$, $gps\_batch\_size$)
        BatchUpdate($\mathcal{G}$, $D_{max}$)
    else
        Update($e$, $D_{max}$)
    end if
end loop
```

that is well within real-time limits for most pose graphs:

$$O(log_b(N)) < C_{max} < O(log_b^2(N)) \tag{3.43}$$

Between these bounds, the actual cost can be chosen at run-time to match the available CPU budget for that frame.

Algorithm 2 AddEdge

```
Input: New edge $e$, connecting nodes $a$ and $b$.
  if neither $a$ nor $b$ are new then
      Add $e$ as a cross-edge.
      if $a$.depth $>$ $b$.depth then
          Swap($a$, $b$)
      end if
      if $b$.depth $>$ $a$.depth $+ 1$ then
          Rebalance($e$, $b$)
      end if
  else
      if $a$ is new then
          Swap($a$, $b$)
      end if
      Add $e$ as a tree edge, making $b$ a child of $a$
  end if
```

3.3.10 Special Considerations for GPS

In some instances, it is desirable to combine omitting nodes and batch-optimizing multiple constraints. For example, we may wish to solve for a locally exact update, by solving for only the nodes close to the robot position, as in [45]. This can be done in our system by omitting faraway nodes, and batch-optimizing all constraints that operate on nearby nodes.

Another application is in the processing of GPS edges. GPS edges are characterized by long path sizes and large position residuals, and do not specify rotation. Relaxing a single GPS constraint c causes its path to bend in order to move the constrained node n closer to the desired position (fig. 3.7). Because c specifies no orientation for the node, n is free to rotate to align itself with the new direction of the path. This is harmful to convergence, as it rotates all of n's sub-tree, increasing the residuals of other GPS constraints, which then do similar damage in turn. To avoid this, we update GPS constraints in batches. This eliminates spurious rotations by placing additional position constraints above n in the tree, preventing the path from bending away from them. We find that relatively small batch sizes are sufficient to prevent spurious rotations. For the Valencia and Paris datasets (section 3.4), we update GPS constraints in batches of 30 and 50, respectively. As when processing other constraints with long paths, we use interpolated solving to keep update times low.

Another concern with GPS edges is that they are a poor choice to use as "tree edges", or edges that connect a parent node to its child. This is because we initialize a new node's pose from its parent's pose by applying the transform of their connecting edge. Doing so with a GPS edge would leave the orientation of the child uninitialized. We need at least one GPS edge in the tree, the one that connects the Earth at the root to the rest of the tree below it. The global orientation of this subtree cannot be determined until we collect three GPS edges, at which point we can initialize it to the orientation that provides the best fit. Only after initializing the global orientation do we relax any GPS edges.

3.3.11 Temperature

To aid convergence, we scale update x_c by a temperature parameter τ, before adding it to parameters z as: $z \leftarrow z + \tau x_c$. We start with $\tau = 1$, and slowly decrease it over time. We do this by scaling τ by 0.99 after each loop through all constraints. If a constraint c's residual is large, the resulting τx_c may contain large rotation updates, which can adversely affect convergence. For such updates, we temporarily substitute τ for a value τ', which is chosen so that the largest rotation update in $\tau' x_c$ does not exceed $\pi/8$.

3.3.12 Choosing edges

When run offline, we relax edges in increasing order of their edge roots. Because relaxing an edge leaves all nodes above the edge root untouched, this ordering serves to reduce oscillation, as relaxing each edge does not undo any work above it in the tree. When performing multiple loops, the edges are looped through in this order.

When running online, the edges are relaxed in the order in which they are added. Surplus CPU time may be spent revisiting old edges according to the user's priorities. A common strategy as employed in Sibley's Relative Bundle Adjustment [45], would be to re-relax local edges to emphasize local consistency.

3.3.13 Algorithm summary

We summarize our method in algorithm 1. The functions "Update" and "BatchUpdate" implement single and multi-constraint updates as described above, using interpolated solving to solve for no more than D_{max} nodes at a time. The "GetUpstreamGPSes(b, n)" function crawls up the tree from node b, and returns the first n GPS edges along that path. In the AddEdge subroutine 2, "Rebalance" is the recursive tree-balancing operation described in section 3.3.9. For simplicity, we have omitted from AddEdge the fact that we replace GPS tree edges with non-GPS edges whenever possible, for reasons described in 3.3.10.

3.4 Results

In this section we report H_2O's performance in the 2011 RSS/WillowGarage SLAM evaluation workshop, demonstrate its convergence on maps from commonly used datasets and Google's Street View database, show the effect of subsampling on convergence quality, and show its robustness to noisy sensor input.

3.4.1 RSS/WillowGarage Automated SLAM Evaluation Workshop results

This algorithm was submitted to the Automated SLAM Evaluation Workshop, held at RSS 2011. On their four benchmark datasets, it competed against other approximate SLAM algorithms HOG-Man [16] and SLoM [21]. It outperformed them in time and χ^2-error on the two 3D datasets, and tied for first place with SLoM overall. We used a maximum domain size D_{max} of 200, and no edge batching.

Full contest details and results may be seen at [26].

3.4.2 Relaxing pose graphs

Fig. 3.8 shows a section of our “Paris1” posegraph before and after optimization, both with and without GPS constraints. We show a case where, without GPS constraints, the optimization causes rotations at an under-constrained intersection, causing the loop to rotate into an unrealistic configuration. We show that GPS constraints serve to limit such error. We also show an instance of the dog-leg problem experienced by TORO. Even though the dog-leg problem is typical with GPS constraints, it can also happen, as it did here, with loop-closing constraints that have a large position residual and small rotation residual. Our method does not suffer from this problem.

In fig. 3.9, we show some maps before and after solving with our method. The “before” images show the poses as initialized by starting at the root of the parametrization tree, and crawling downwards, concatenating the tree edges’ transforms. For a pose graph with no loop closures, this would be equivalent to dead-reckoning. The red edges are edge residuals, connecting the desired pose of a node to its actual pose. Relative constraints’ residuals connect two poses, while GPS constraints’ residuals connect a pose to a spot in empty space, indicating the desired position. Redder residuals indicate higher error. Longer residuals do not necessarily have higher error, as some edges are less stiff than others. In particular, GPS constraints are much less stiff than other types, due to GPS’ imprecision. Our method performs well on graphs with ample loop closures, such as Olson’s “Manhattan world”, converging to an average energy per constraint of 1.596, compared to TORO’s 2.062. Our method completely collapses most relative constraint residuals (fig. 3.9b, 3.9d), and greatly reduces GPS residuals (fig. 3.9f). A small number of lines which overlap in fig. 3.9e can be seen to have split apart in 3.9f. These are parallel runs where the loop closure detector failed to recognize as traversing the same path, and therefore did not connect together with a constraint. Outdoor urban maps can have fewer loop-closures, due to the difficulty of detecting them in highly dynamic environments. Despite this distortion, the solved map aligns relatively well to satellite photography, as seen in fig. 3.10.

3.4.3 Convergence

In fig. 3.11, we show the log-energy per constraint over time for our method and TORO. Our method reduces the error quicker, and converges to an average energy per constraint that is an order of magnitude lower than that of TORO. For our method, we use interpolated solving as described in section 3.3.6, with different maximum values D_{max} for the size of set $\mathcal{S}_c$. GPS constraints were not used, to minimize dog-legs in TORO. The pose graph data was taken from a section of Valencia, Spain, with 15031 poses and 15153 constraints. The energy was measured after each loop through all constraints. In actual operation, only a few constraints are added or updated per frame, so the spacing of the points in the plot should not be interpreted as the required time per iteration. Rather, see table 3.2 for the average and maximum time per constraint for the same solvers and posegraph. The average constraint domain size was 1.53 poses, while the largest constraint domain was 1161 poses. The times shown are all within real-time bounds per frame, except when domain subsampling is turned off (by setting $D_{max} = \infty$).

Linearizing the relation between position error and rotation updates is neces-

Table 3.2: Average and maximum time per constraint, Valencia dataset

Solver	Avg. time (s)	Max. time (s)
TORO	$1.75092 * 10^{-5}$	$5.24759 * 10^{-3}$
$D_{max} = 75$	$3.6635 * 10^{-4}$	$5.3559 * 10^{-2}$
$D_{max} = 100$	$4.0791 * 10^{-4}$	$6.5095 * 10^{-2}$
$D_{max} = 150$	$4.919 * 10^{-4}$	$9.5015 * 10^{-2}$
$D_{max} = 200$	$5.812 * 10^{-4}$	0.13747
$D_{max} = \infty$	$2.0823 * 10^{-3}$	3.583

sary for properly addressing the dog-leg problem. However, such projective rotations can also cause oscillations in the face of excessive subsampling. To test our method's robustness to oscillations, we ran the solver with various levels of subsampling, defined by D_{max}, the maximum number of nodes to solve for in (3.39). Table 3.1 shows the minimum values of D_{max} which did not cause divergence. Note that these are not hard minimums, as divergence may also be avoided by lowering the initial temperature τ from 1.0. This table is only intended to illustrate the potential danger of over-subsampling. Table 3.1 also shows each map's number of nodes, edges, loop edges, and maximum domain size ("max d"). Loop edges are edges with more than two nodes in their path (they are also counted under "edges"). The "Manhattan world" dataset was originally used by Olson in [38] (see fig. 3.9a).

In fig. 3.11, we compare online and offline operation of H_2O. The first iteration of the online hybrid hessian run is delayed (shifted to the right) due to the overhead incurred by the dynamic tree balancing described in section 3.3.9.

3.4.4 Robustness to noise

To test the robustness of our solver to large errors due to sensor noise, we added rotational noise to all edges in the "Manhattan world", Valencia, and Paris2 pose graphs. These “noisified” graphs can be seen in fig. 3.12. Each rotation was multiplied by a small rotation around the local up axis, where the angle was drawn from a normal distribution with a standard deviation of 3 degrees. When the poses are initialized using these edges, these small rotations add up to the large map distortions shown in the left column.

3.5 Conclusions and Future Work

We have described a method for online SLAM which combines strengths from stochastic and exact approaches, and provides a means of controlling the exactness and cost of a given SLAM update. Like previous stochastic methods, our method exhibits fast-converging updates and robustness to large initialization errors. Like exact methods, we are able to process GPS constraints without introducing the pose staggering known as the “dog-leg problem”, previously a weakness of stochastic methods. We demonstrated a means of reducing the complexity of updates in order to stay within real-time bounds on every update, so as not to disrupt higher-level operations with cost spikes. In addition, we demonstrated batch-optimizing multiple constraints, with applications to stable GPS updates. Taken together, these techniques allow the user to smoothly transition between approximate $O(n)$-per-constraint loop closing (where n is the size of the constraint's loop), and exact updates as used by exact solvers. Our algorithm optimizes to a lower overall energy than a state-of-the-art method in stochastic SLAM, while staying well within real-time cost bounds per constraint. We have presented a means of dynamically balancing a parametrization tree to minimize the worst-case cost of future loop-closures. Finally, we demonstrated a simple scheme of row and column ordering to ease batch-solving multiple constraints.

In the future, we would like to investigate using spare CPU time to relax old edges. How to select which edge to revisit, and how to minimize disruptions to its nodes' subtrees, remain open questions. To that end, a remaining problem with our method is that old nodes higher up in the pose tree become resistant to change, as newer edges add to those nodes' corresponding values in the regularizer B. This can make relaxing old sections of the pose graph resistant to change. Further investigation is necessary to selectively "un-stiffen" parts of the old graph in response to new information.

Reordering the columns and rows when batch-relaxing edges is another topic with room for exploration. Our tree parametrization results in groups of rows with similar sparsity patterns, making them amenable to supernodal approaches to QR factorization [8].

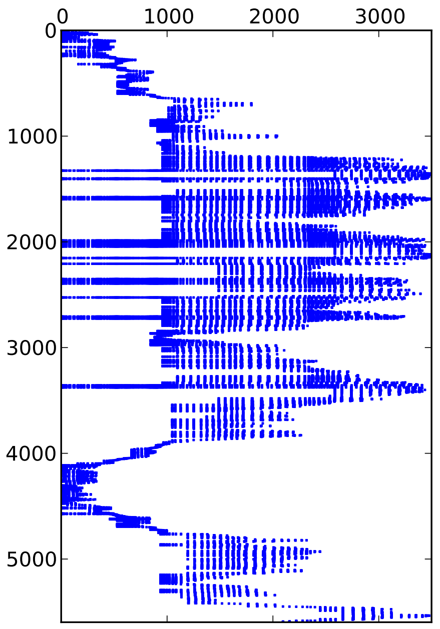

(a) J matrix

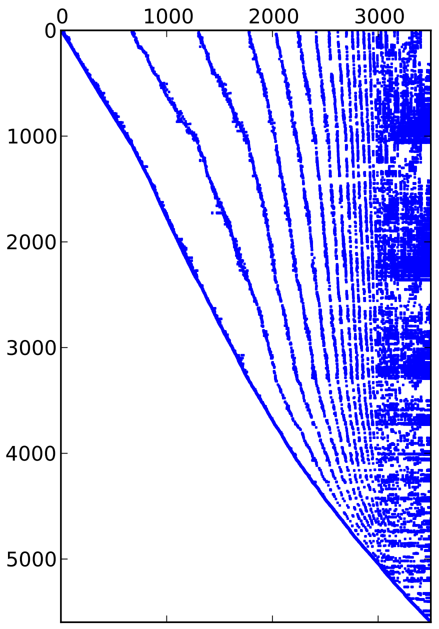

(b) J, reordered

Figure 3.5: **Reordering edges and nodes:** The sparsity pattern of the full square-root information matrix (J) of the Manhattan dataset [37], constructed from all of the edges. Each column corresponds to a node (pose), while each row corresponds to an edge (sensor reading). In fig. 3.5a, the rows and columns are listed in chronological order of their corresponding sensor readings and poses. In fig. 3.5b, they are sorted as described in section 3.3.8. This matrix has fewer sub-diagonal elements, making it easier to upper-triangularize and solve. The left matrix took 41.52 seconds to QR-factorize with Householder reflections on a 2 GHz Intel Core 2 Duo; the right matrix took 12.26 seconds.

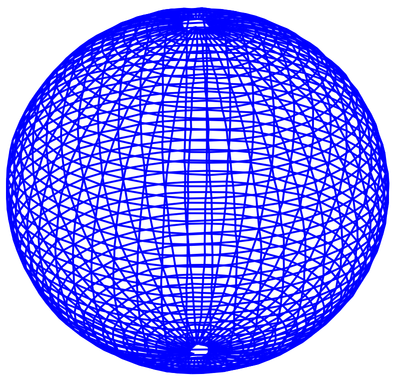

(a) Pose graph (2500 nodes)

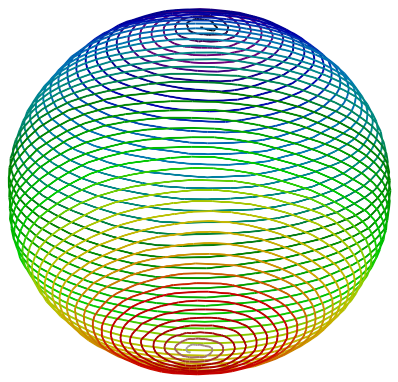

(b) Naive tree ($d_{max} = 2500$)

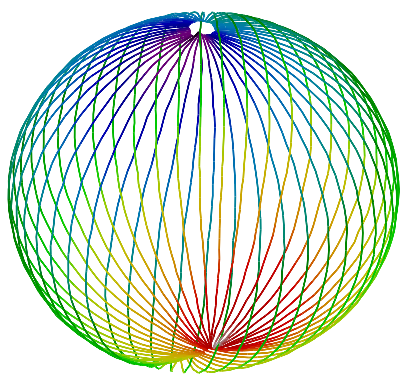

(c) BFT (offline, $d_{max} = 50$)

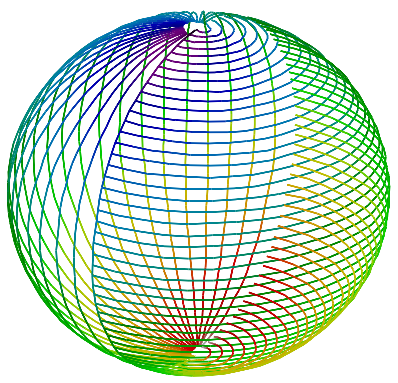

(d) Online balancing ($d_{max} = 50$)

Figure 3.6: **Online tree balancing.** From left to right: fig. 3.6a shows the sphere dataset [17], a pose graph formed by a robot spiraling down a sphere from top to bottom. The remaining figures show various spanning trees, where tree depth is indicated by color (redder is deeper). Figure 3.6b shows a pathological case of naive tree growth, in which old nodes never change parents. Online TORO and SGD use this method. Fig. 3.6c shows a tree built offline by simple breadth-first traversal of the graph, as employed in [15]. This guarantees a balanced tree, but can only be done offline, not online. Fig. 3.6d shows the tree when using dynamic balancing, as described in section 3.3.9.

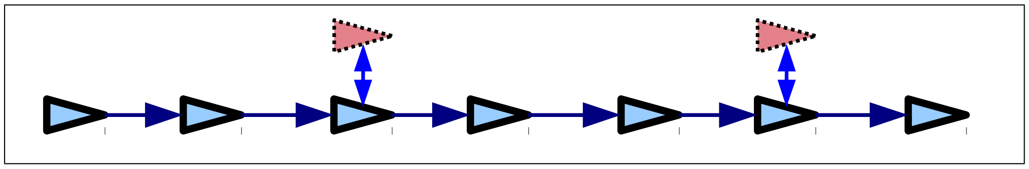

(a) Two GPS constraints

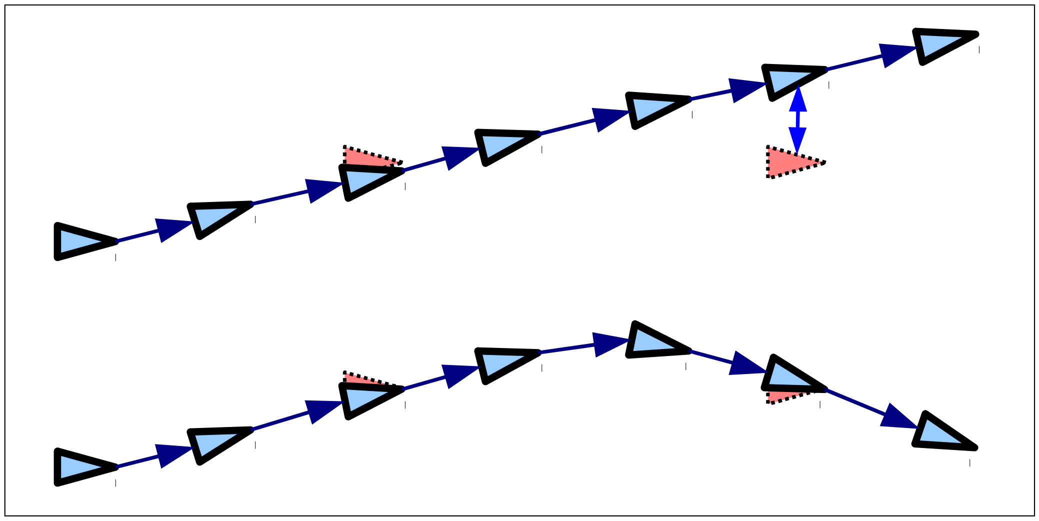

(b) Relaxing them sequentially

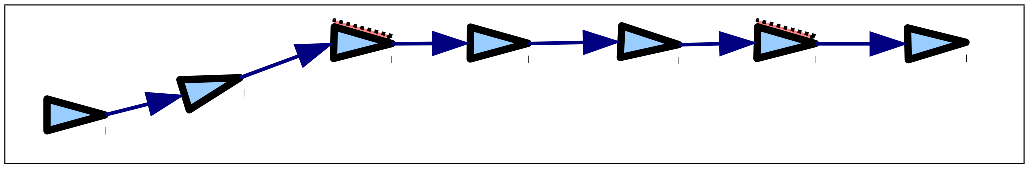

(c) Batch-relaxing them together

Figure 3.7: **Batch-relaxing GPS** Because GPS constraints do not specify rotation, relaxing them one at a time can cause spurious rotations of the constrained node and its subtree. To lock down rotation, we relax them together in a batch.

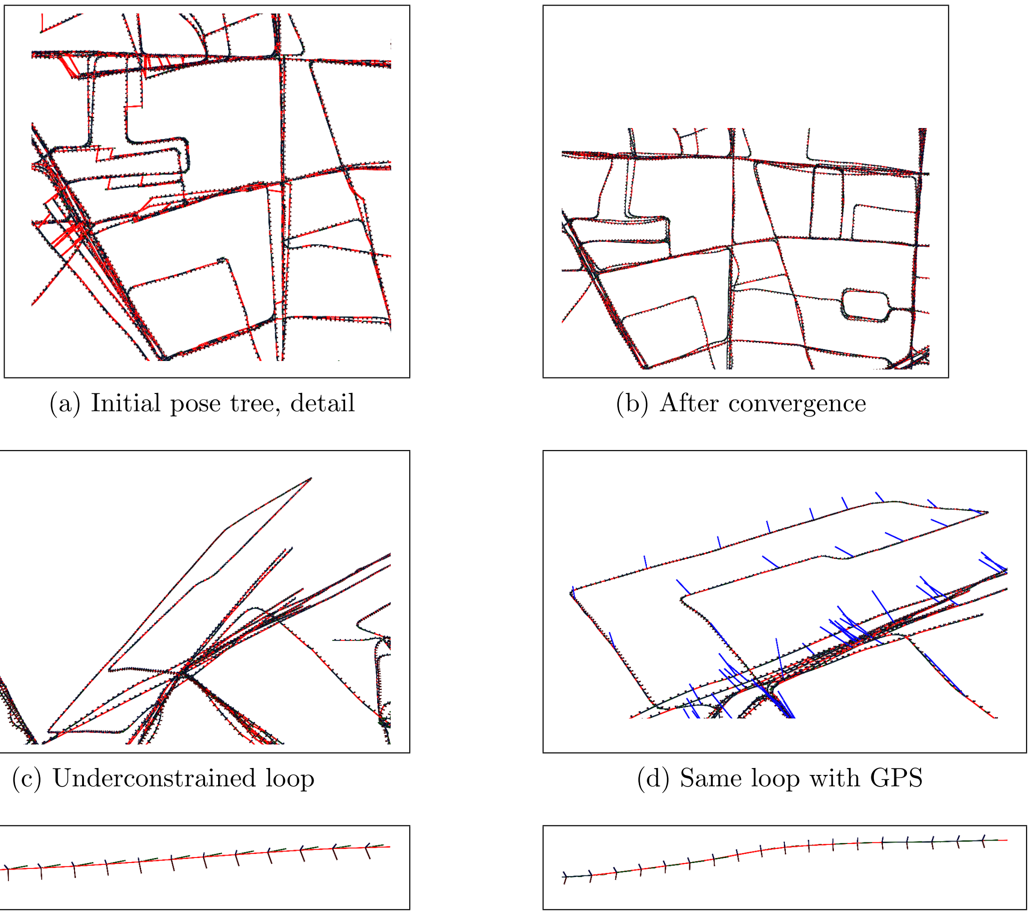

(a) Initial pose tree, detail

(b) After convergence

(c) Underconstrained loop

(d) Same loop with GPS

(e) Dog-legged path, after convergence with TORO

(f) Same path, after convergence with our method

Figure 3.8: **Paris1 dataset** A posegraph taken from a section of Paris, with 27093 nodes and 27716 constraints. Fig. 3.8a shows a section of the pose tree in its initial state. Stretched constraints can be seen as red lines. Fig. 3.8b is the same section after 10 iterations of our method, using a maximum problem size of $D_{max} = 200$, and no GPS constraints. The stretched constraints of 3.8a have collapsed; the runs that remain separated are those without constraints tying them together. Fig. 3.8c shows a severely under-constrained intersection, with few loop-closing constraints connecting adjacent runs. Such intersections can happen due to the difficulty in identifying loop closures in dynamic urban environments. While optimizing the posegraph, parallel paths with no cross-connections can become separated. Fig. 3.8d shows the same intersection when GPS constraints are added to one out of every 100 nodes. The GPS' residual vectors are visible as blue line segments. Unlike loop-closing constraints, GPS constraints are easy to come by, limit drift in large loops, and prevent separation of nearby unconnected runs. Fig. 3.8e shows a portion of the Paris posegraph after convergence with TORO. The dog-leg problem has caused the vehicle poses to not point along the direction of travel. No GPS constraints were used. Fig. 3.8f shows the same portion, after convergence with our method.

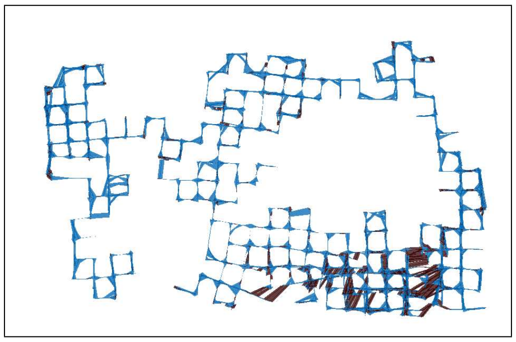

(a) Olson's "Manhattan world"

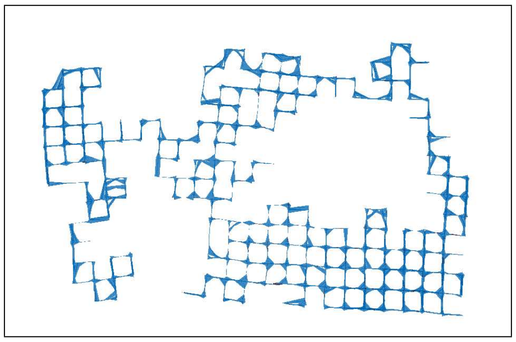

(b) "Manhattan world", converged

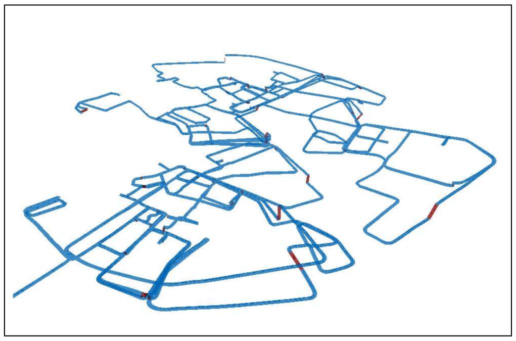

(c) Valencia

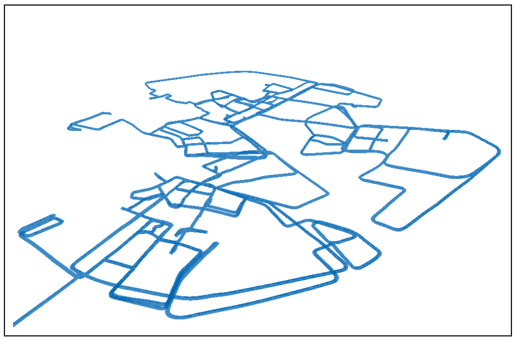

(d) Valencia, converged

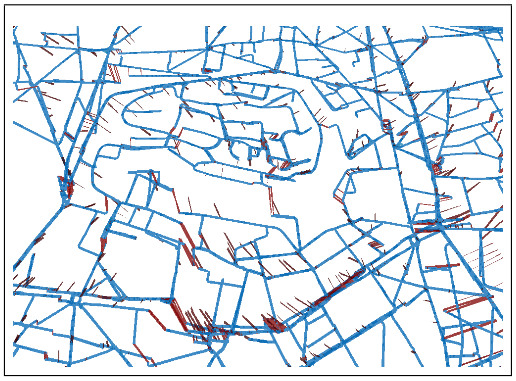

(e) Paris2

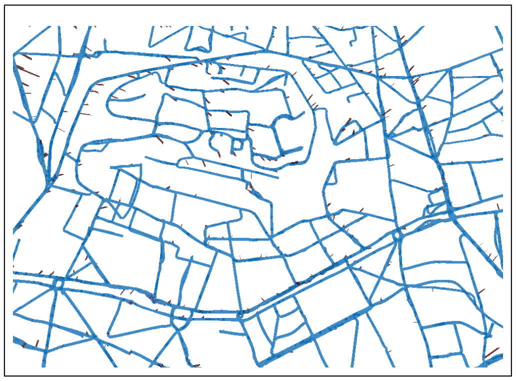

(f) Paris2, converged

Figure 3.9: **Solved maps** Pose graphs, before and after 10 iterations with $D_{max} = 200$. Pose graph sizes are given in table 3.1. Initial configurations show the poses as set by concatenating constraint transforms down the tree, as described in section 3.3.2. Constraint residuals are shown as brown/red lines connecting the constraint's desired pose to the actual pose. Brighter red indicates higher error. Valencia (fig. 3.9c, fig. 3.9d) is shown at an oblique angle, to better show its error residuals, which are primarily vertical.

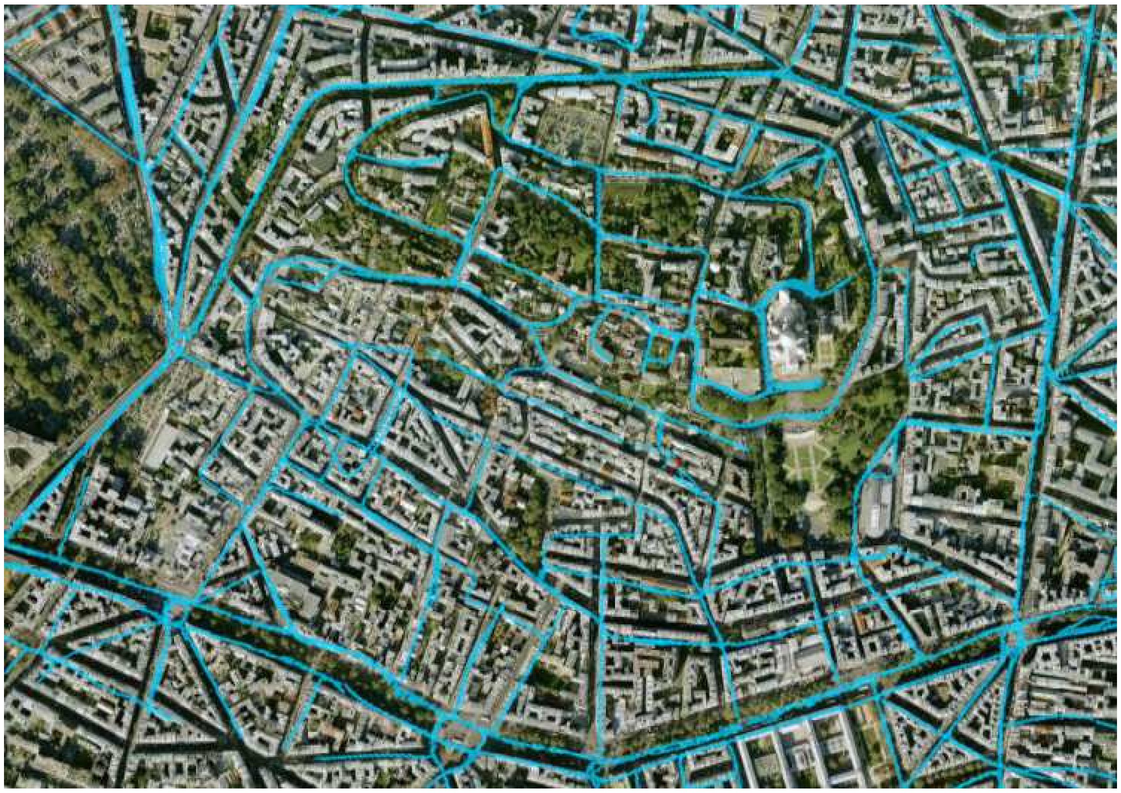

Figure 3.10: **Montmartre, Paris** An overlay of the converged poses of fig. 3.9f on a satellite image from Google Earth.

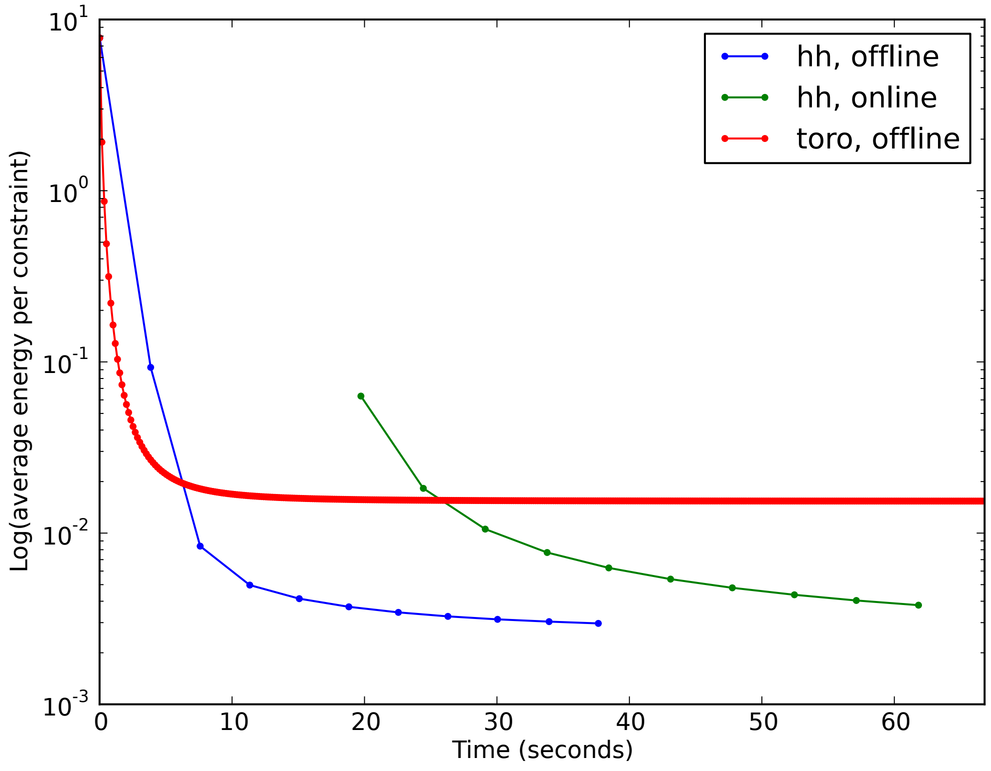

Figure 3.11: **Online vs offline convergence** Online tree-balancing incurs some additional cost over offline operation, as shown by the rightward shift of the green line (online) relative to the blue line (offline). Each point represents a complete loop through all edges. After the first loop, the online algorithm revisits old edges in depth-first order.

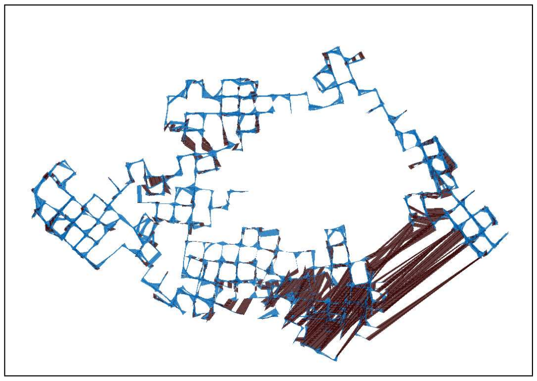
(a) "Manhattan world", noisified

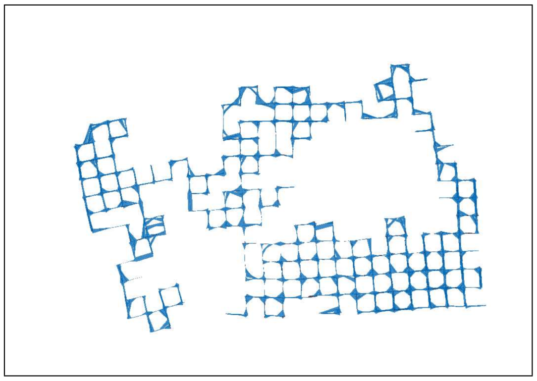
(b) "Manhattan world", converged

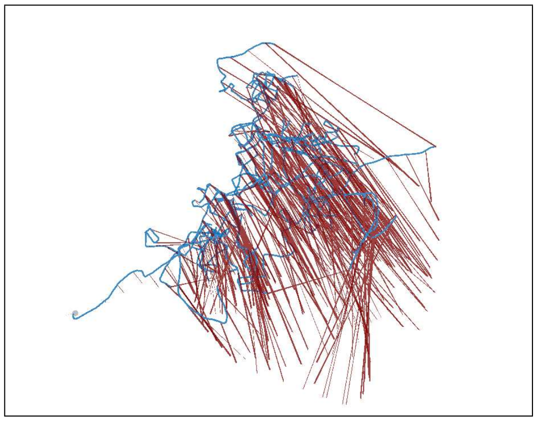
(c) Valencia, noisified

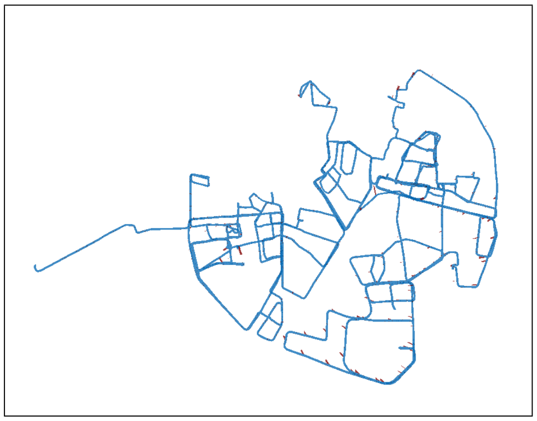
(d) Valencia, converged

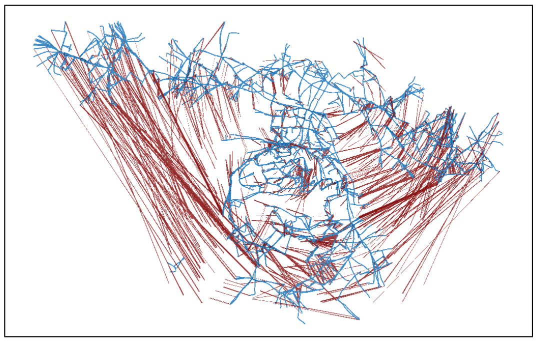
(e) Paris2, noisified

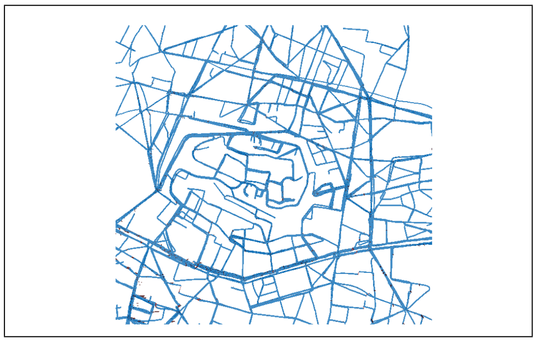
(f) Paris2, converged

Figure 3.12: **Graphs with large initial error** Pose graphs, with noisified constraints (sensor readings). A small random rotation around the local up axis was multiplied onto each constraint's rotation, causing large distortions to accumulate over time. Pose graph sizes given in table 3.1. Constraint residuals are shown as brown/red lines (redder = more error).

4
Conclusions and Future Work

SLAM solvers have rightly aspired to be a black box: a general purpose tool that offers few controls, and in turn asks few questions of the work to which it is put. Unfortunately, making localizers insensitive to their context can make them much more expensive than necessary. The efficiency loss can be great enough to impact the overall capability of the robot. In chapter 2, it made the difference between being able to afford a long-distance vision module, or not. In chapter 3, it determined whether SLAM could guarantee real-time operation, or not. When the expense of a black box affects high-level design decisions, it is no longer a black box.

In localization, speed and accuracy are competing priorities. Many localizers seek to distinguish themselves by optimizing for one or the other. This thesis argues that a localizer should instead position itself between these priorities in a way that best serves the task at hand.

Chapter 2 showed that by combining wheel odometry and visual odometry, one may achieve comparable accuracy to pure visual odometry at 5 percent of the cost. Hybridizing the two odometry types eliminates their biggest problems, namely hallucinated rotations caused by wheel slip, and processor saturation caused by the high cost of pure visual odometry.

Chapter 3 described H_2O, a SLAM solver which can dynamically adjust between exact accuracy and fast linear-time speed. This provides a unique control knob. It allows the robot to dictate the computational budget of SLAM, rather than the other way around. This enables SLAM to remain unobtrusive to the rest of the robot's system, as a black box should. At its fastest and least accurate setting, our solver converges faster than the fastest competing SLAM solver, with a χ^2-error that is lower by a factor of 10. At its most accurate setting, H_2O matches the error of exact SLAM solvers.

There is room to improve H_2O along its two primary strengths: cost, and flexibility. H_2O already boasts very fast loop-closing times, but pushing the speed too far can harm convergence. This limit is currently determined empirically. We expect that with further study, we will be able to determine this limit for a loop before actually solving it, thus enabling us to make loop closures as fast as is sensible, but no faster. Another strength of H_2O is its flexibility: the user may choose which poses and edges to solve for. This allows for useful optimizations, such as solving only for poses close to the robot, for example. While useful, such arbitrary relaxations are more likely to introduce discontinuities in the map, as compared to the default usage of relaxing the most recently added edge. Studying how to prevent such discontinuities, and how to most efficiently repair them when they occur, will further enhance H_2O's flexibility.

A

Differentiating Hierarchical Poses

Hierarchical trees of rigid-body transforms find use in many problems, such as inverse kinematics, segmented limb control, and as seen in this thesis, SLAM. Such problems often optimize some error function of pose, requiring us to differentiate this pose with respect to the chain of transforms from which it is formed. Resources that describe the necessary calculus in sufficient detail remain surprisingly hard to find. This appendix presents a complete derivation, for the benefit of implementors.

Notation

In this section, we consider a chain of tranforms from node 0 (the root of the pose tree) down to a node N, using the following conventions and symbols.

Conventions

- All vectors are column vectors.
- Quaternions are laid out as $[\begin{array}{cccc} w & x & y & z \end{array}]$.
- If $x = [\begin{array}{ccc} x_1 & \cdots & x_m \end{array}]$ and $y = [\begin{array}{ccc} y_1 & \cdots & y_n \end{array}]$, the derivative $\frac{\partial x}{\partial y}$ is a $m \times n$ matrix where the element at row r and column c stores $\frac{\partial x_r}{\partial y_c}$.
- Given a quaternion q and 3-D vector v, the notation qv expresses a quaternion product between q and the quaternion $[\begin{array}{cc} 0 & v \end{array}]$.

Symbols

t_n, q_n	Relative translation and rotation quaternion from pose n-1 to n.
x_n, r_n	Global position and rotation quaternion of pose n (A.3).
Q_n, R_n	Rotation matrix representation of quaternions q_n, r_n (A.5).
$f(v, q)$	Vector v, rotated by quaternion q. Defined as qvq^{-1}, equal to Qv.
q_I, I	Identity quaternion $[\begin{array}{cccc} 1 & 0 & 0 & 0 \end{array}]$, and the identity 3×3 matrix.
Mq	Quaternion q, treated as a vector, multiplied with matrix M.
$M \otimes q$	Quaternion-multiplication of the columns of M, with q (A.1, A.2).

Let M be a 4×4 matrix. Writing M's columns as $M = \left[\begin{array}{cccc} c_0 & c_1 & c_2 & c_3 \end{array}\right]$, we define $\otimes$ using columnwise quaternion multiplication:

$$M \otimes q = \left[\begin{array}{cccc} c_0 q & c_1 q & c_2 q & c_3 q \end{array} \right] \tag{A.1}$$

$$q \otimes M = \left[\begin{array}{cccc} q c_0 & q c_1 & q c_2 & q c_3 \end{array} \right] \tag{A.2}$$

Kinematic chain notation

There are various notational conventions for chaining rigid body transformations. We illustrate ours by spelling out the expressions for global poses 0 through 3:

$$\begin{aligned}
r_0 &= q_0 & x_0 &= t_0 \\
r_1 &= q_0 q_1 & x_1 &= t_0 + f(t_1, q_0) \\
r_2 &= q_0 q_1 q_2 & x_2 &= t_0 + f(t_1, q_0) + f(t_2, q_0 q_1) \\
r_3 &= q_0 q_1 q_2 q_3 & x_3 &= t_0 + f(t_1, q_0) + f(t_2, q_0 q_1) + f(t_3, q_0 q_1 q_2)
\end{aligned}$$

If we define r_{-1} to be the identity rotation, we may write the n'th global pose as:

$$r_n = \prod_{i=0}^{n} q_i \tag{A.3}$$

$$x_n = \sum_{i=0}^{n} f(t_i, r_{i-1}) \tag{A.4}$$

or using matrix notation:

$$R_n = \prod_{i=0}^{n} Q_i \tag{A.5}$$

$$x_n = \sum_{i=0}^{n} R_{i-1} t_i \tag{A.6}$$

Differentiating Global Poses

We wish to modify the local transforms to minimize some convex error function $E(x_n, r_n)$ of the global pose at the end of the chain. We start by taking the gradients with respect to t_i and q_i :

$$\frac{\partial E}{\partial t_i} = \frac{\partial E}{\partial x_n}\frac{\partial x_n}{\partial t_i} + \frac{\partial E}{\partial r_n}\cancelto{0}{\frac{\partial r_n}{\partial t_i}} \tag{A.7}$$

$$\frac{\partial E}{\partial q_i} = \frac{\partial E}{\partial x_n}\frac{\partial x_n}{\partial q_i} + \frac{\partial E}{\partial r_n}\frac{\partial r_n}{\partial q_i} \tag{A.8}$$

We note from (A.3) that the Jacobian $\frac{\partial r_n}{\partial t_i}$ is zero, hence its cancellation in (A.7) above. The remainder of this section will derive the remaining Jacobians $\frac{\partial x_n}{\partial t_i}$, $\frac{\partial x_n}{\partial q_i}$, and $\frac{\partial r_n}{\partial q_i}$.

Global position with respect to local translation

The Jacobian with respect to the local translation t_i is simple. Differentiating both sides of (A.6), all but the i'th term in the sum drop out to yield:

$$\frac{\partial x_n}{\partial t_i} = R_{i-1}\frac{\partial t_i}{\partial t_i} \tag{A.9}$$

$$= R_{i-1} I \tag{A.10}$$

Thus:

$$\boxed{\frac{\partial x_n}{\partial t_i} = R_{i-1}} \tag{A.11}$$

As one might expect, this shows that variations of t_i can be mapped to variations of x_n by R_{i-1}, the global orientation of the pose just above t_i in the kinematic chain.

Global position with respect to local rotation

The Jacobian of global position x_n with respect to the local rotation q_i is more involved. In fact, we will show that it is more convenient to derive the Jacobian in a rotated coordinate frame where $q_i = q_I$. We will then use this Jacobian to update the transformed q_i, then transform the updated q_i back to its original coordinate frame.

We start by differentiating both sides of (A.6):

$$\frac{\partial x_n}{\partial q_i} = \frac{\partial}{\partial q_i} \sum_{j=0}^{n} R_{j-1} t_j \tag{A.12}$$

We can drop all terms in the sum that do not contain q_i to get:

$$\frac{\partial x_n}{\partial q_i} = \frac{\partial}{\partial q_i} \sum_{j=i+1}^{n} R_{j-1} t_j \tag{A.13}$$

$$= \sum_{j=i+1}^{n} \frac{\partial}{\partial q_i} R_{j-1} t_j \tag{A.14}$$

$$= \sum_{j=i+1}^{n} \frac{\partial}{\partial q_i} \left(\prod_{k=0}^{j-1} Q_k \right) t_j \tag{A.15}$$

$$= \sum_{j=i+1}^{n} \left(\prod_{k=0}^{i-1} Q_k \right) \frac{\partial}{\partial q_i} \left(\prod_{l=i}^{j-1} Q_l \right) t_j \tag{A.16}$$

$$= \sum_{j=i+1}^{n} R_{i-1} \frac{\partial}{\partial q_i} \left(\prod_{l=i}^{j-1} Q_l \right) t_j \tag{A.17}$$

According to Wheeler and Ikeuchi [53], the Jacobian of a rotated vector $f(v, q)$ with respect to the rotating quaternion q takes a particularly simple form when $q = q_I$, the identity:

$$\left. \frac{\partial f(v, q)}{\partial q} \right|_{q=q_I} = \begin{bmatrix} 0 & 0 & 2z & -2y \\ 0 & -2z & 0 & 2x \\ 0 & 2y & -2x & 0 \end{bmatrix} \tag{A.18}$$

where

$$[\ x \quad y \quad z\ ] = f(v, q) \tag{A.19}$$

This handy fact can be applied to any value of q and v, by rotating them into a frame where $q = q_I$:

$$v' = f(v, q) \tag{A.20}$$

$$q' = q_I \tag{A.21}$$

In (A.17), we perform a similar change of variables from t_j and q_i:

$$t'_j = \left(\prod_{l=i}^{j-1} Q_l \right) t_j \tag{A.22}$$

$$q'_i = q_I \tag{A.23}$$

This yields an expression for $\frac{\partial x_n}{\partial q'_i}$:

$$\boxed{\frac{\partial x_n}{\partial q'_i} = \sum_{j=i+1}^{n} R_{i-1} \frac{\partial t'_j}{\partial q'_i}} \tag{A.24}$$

Where $\frac{\partial t'_j}{\partial q'_i}$ is given by plugging in $[t'_j = \begin{matrix} x & y & z \end{matrix}]$ into (A.18).

Given the Jacobian $\frac{\partial x_n}{\partial q'_i}$, we can solve for a step $\Delta q'_i$ for q'_i using whatever gradient-based nonlinear optimization algorithm we choose. The linearized update to q'_i is:

$$q'_i \leftarrow (q'_i + \Delta q'_i)/||q'_i + \Delta q'_i|| \tag{A.25}$$

Note the normalization, done to ensure that q'_i remains a pure rotation with no scaling. To transform the updated q'_i back to the original unrotated coordinate frame q_i, we use the definition:

$$q_i = q_c q'_i \tag{A.26}$$

Here q_c is the value of q_i before the update step.

Finally, we pause to note one feature of the Jacobian $\frac{\partial v'}{\partial q'}$ given by (A.18), namely that its first column is all zeros. This column corresponds to variations in the first element of q'. Intuitively, this means that any gradient descent step $\Delta q'$ that simply scales the current value of $q' = [\begin{array}{cccc} 1 & 0 & 0 & 0 \end{array}]$ without changing the rotation it represents will have no effect on $f(v', q')$. Conversely, using this Jacobian to calculate a step $\Delta q'$ will not move q in such useless directions. This relieves us of having to impose extra constraints, such as Lagrange multipliers, on q'. We do still need to normalize q' after the update, as $q' + \Delta q'$ may not be unit length.

Global rotation with respect to local translation

By inspection of (A.3), we see that global rotation does not depend on local translation:

$$\boxed{\frac{\partial r_n}{\partial t_i} = \begin{bmatrix} 0 & 0 & 0 \\ 0 & 0 & 0 \\ 0 & 0 & 0 \\ 0 & 0 & 0 \end{bmatrix}} \tag{A.27}$$

Global rotation with respect to local rotation

Global rotation r_n is a product of a chain of local rotations:

$$r_n = \prod_{j=0}^{n} q_j \qquad \text{From (A.3)} \tag{A.28}$$

We would like to differentiate r_n with respect to one of these local rotations, q_i. We start by multiplying together all rotations above q_i in the chain, and similarly, all rotations below q_i. We call these products q_a and q_b:

$$r_n = \left(\prod_{j=0}^{i-1} q_j\right) q_i \left(\prod_{k=i+1}^{n} q_k\right) \tag{A.29}$$

$$= q_a q_i q_b \tag{A.30}$$

Differentiating (A.30) with respect to q_i, we get:

$$\frac{\partial r_n}{\partial q_i} = q_a \otimes I \otimes q_b \tag{A.31}$$

where I is a 4×4 identity matrix, and we use $\otimes$ to denote columnwise quaternion multiplication. In other words, the c'th column of $\frac{\partial r_n}{\partial q_i}$ is the quaternion product $q_a I_c q_b$, where I_c is the c'th column of I.

If we are to use this $\partial r_n/\partial q_i$ alongside $\partial x_n/\partial q_i'$ from section A, we need to modify it to use the transformed rotations q_i' rather than q_i. This is easily done by plugging $q_i = q_c q_i'$ (A.26) into (A.29):

$$r_n = \left(\prod_{j=0}^{i-1} q_j\right) q_i \left(\prod_{k=i+1}^{n} q_k\right) \tag{A.32}$$

$$= \left(\prod_{j=0}^{i} q_j\right) q_i' \left(\prod_{k=i+1}^{n} q_k\right) \tag{A.33}$$

$$= q_a' q_i' q_c \tag{A.34}$$

where

$$q'_a = \left(\prod_{j=0}^{i} q_j\right) \tag{A.35}$$

$$q'_i = q_I \tag{A.36}$$

As with (A.31), we differentiate both sides of (A.34) to get:

$$\boxed{\frac{\partial r_n}{\partial q'_i} = q'_a \otimes I \otimes q_b} \tag{A.37}$$

Differentiating Relative Poses

Instead of minimizing an energy function of a global pose, we may want to minimize an energy function of the relative pose between two global poses $[x_a, r_a]$ and $[x_b, r_b]$. In this section we differentiate this relative transform $[t_{ab}, q_{ab}]$ with respect to the hierarchical transforms $[t_i, q_i]$.

While the following equations are written in terms of “global poses” $[x_i, r_i]$, there is no special requirement that the poses be in the coordinate frame of the pose tree’s root. Any consistent reference frame will yield the same results. In practice, we use the reference frame of lowest common ancestor of poses a and b in the pose tree.

Relative translation with respect to local translation

The relative translation t_{ab} is given by:

$$t_{ab} = f(x_b - x_a, r_a^{-1}) \tag{A.38}$$

$$= R_a^{-1}(x_b - x_a) \tag{A.39}$$

Differentiating both sides with respect to t_i gets:

$$\boxed{\frac{\partial t_{ab}}{\partial t_i} = R_a^{-1}\left(\frac{\partial x_b}{\partial t_i} - \frac{\partial x_a}{\partial t_i}\right)} \tag{A.40}$$

The derivatives $\frac{\partial x_b}{\partial t_i}$ and $\frac{\partial x_a}{\partial t_i}$ are given by (A.11). We treat R_a^{-1} as a constant in the above differentiation, since global rotations are independent of local translations (A.5).

Relative translation with respect to local rotation

Differentiating the relative translation t_{ab} (A.38) with respect to the local rotation q_i' yields:

$$\frac{\partial t_{ab}}{\partial q_i'} = \frac{\partial}{\partial q_i'} f(x_b - x_a, r_a^{-1}) \tag{A.41}$$

$$= \frac{\partial}{\partial q_i'} r_a(x_b - x_a)r_a^{-1} \tag{A.42}$$

$$\begin{aligned} = \; & \frac{\partial r_a}{\partial q_i'} \otimes (x_b - x_a)r_a^{-1} \qquad (A.43) \\ & + r_a \otimes \left(\frac{\partial x_b}{\partial q_i'} - \frac{\partial x_a}{\partial q_i'}\right) \otimes r_a^{-1} \\ & + r_a(x_b - x_a) \otimes \frac{\partial r_a^{-1}}{\partial q_i'} \end{aligned}$$

Expanding the $\partial r_a^{-1}/\partial q_i'$ in the last term above gets:

$$\begin{aligned}
\frac{\partial r_a^{-1}}{\partial q_i'} &= \frac{\partial r_a^{-1}}{\partial r_a}\frac{\partial r_a}{\partial q_i'} && \text{(A.44)}\\
&= \frac{\partial r_a^{*}}{\partial r_a}\frac{\partial r_a}{\partial q_i'} \qquad r^{-1} = r^* \text{ because } r \text{ is unit length} && \text{(A.45)}\\
&= I^*\frac{\partial r_a}{\partial q_i'} && \text{(A.46)}
\end{aligned}$$

where

$$I^* = \begin{bmatrix} 1 & 0 & 0 & 0 \\ 0 & -1 & 0 & 0 \\ 0 & 0 & -1 & 0 \\ 0 & 0 & 0 & -1 \end{bmatrix} \tag{A.47}$$

Therefore:

$$\boxed{\begin{aligned}
\frac{\partial t_{ab}}{\partial q_i'} =& \frac{\partial r_a}{\partial q_i'} \otimes (x_b - x_a) r_a^{-1} \\
&+ r_a \otimes \left(\frac{\partial x_b}{\partial q_i'} - \frac{\partial x_a}{\partial q_i'}\right) \otimes r_a^{-1} \\
&+ r_a (x_b - x_a) \otimes I^* \frac{\partial r_a}{\partial q_i'}
\end{aligned}} \tag{A.48}$$

The $\frac{\partial r_n}{\partial q_i'}$ derivative is given by (A.37), while $\frac{\partial x_b}{\partial t_i}$ and $\frac{\partial x_a}{\partial t_i}$ are given by (A.11). The $\left(\frac{\partial x_b}{\partial q_i'} - \frac{\partial x_a}{\partial q_i'}\right)$ term is a 3×4 matrix, whose 3-D columns are multiplied by quaternions r_a and r_a^{-1}. As when quaternion-multiplying 3-D position vectors, this is done by padding the columns with leading zeros. The product is a 4×4 matrix with zeros in the first row. The remaining two terms above have first rows which cancel out to zero when added together. The entire right-hand side therefore resolves to a 4×4 matrix with a zero first row. The remaining three rows are written to the left-hand side, the 3×4 matrix $\frac{\partial t_{ab}}{\partial q_i'}$.

Relative rotation with respect to local translation

The relative rotation between global poses $[x_a, r_a]$ and $[x_b, r_b]$ is given by:

$$q_{ab} = r_a^{-1} r_b \tag{A.49}$$

As when deriving $\partial r/\partial t$, we note from (A.3) that the global rotations r_a and r_b are independent from local translations t_i. Therefore,

$$\boxed{\frac{\partial q_{ab}}{\partial t_i} = \begin{bmatrix} 0 & 0 & 0 \\ 0 & 0 & 0 \\ 0 & 0 & 0 \\ 0 & 0 & 0 \end{bmatrix}} \tag{A.50}$$

Relative rotation with respect to local rotation

Differentiating both sides of A.49 we get:

$$\frac{\partial q_{ab}}{\partial q_i'} = \frac{\partial r_a^{-1}}{\partial q_i'} \otimes r_b + r_a^{-1} \otimes \frac{\partial r_b}{\partial q_i'} \tag{A.51}$$

$$= \frac{\partial r_a^{-1}}{\partial r_a} \frac{\partial r_a}{\partial q_i'} \otimes r_b + r_a^{-1} \otimes \frac{\partial r_b}{\partial q_i'} \tag{A.52}$$

Plugging in $\frac{\partial r_a^{-1}}{\partial r_a} = I^*$ (A.47) we get:

$$\boxed{\frac{\partial q_{ab}}{\partial q_i'} = I^* \frac{\partial r_a}{\partial q_i'} \otimes r_b + r_a^{-1} \otimes \frac{\partial r_b}{\partial q_i'}} \tag{A.53}$$

where the $\frac{\partial r}{\partial q'}$ terms are given by (A.37).

B

Constraint Jacobians

Here we show how to calculate the jacobians of arbitrary sensor types, so that they may be used in graphical SLAM methods, such as the H_2O algorithm of chapter 3.

Constraint functions

Most graphical SLAM methods, including H_2O, model edges as quadratic penalty functions between an observed value k and a prediction function $g(z)$, which predicts the expected observed value, given state z:

$$\begin{aligned} E &= ||g(z) - k||_\Omega && \text{(B.1)} \\ &= (g(z) - k)^T \Omega^{-1} (g(z) - k) && \text{(B.2)} \end{aligned}$$

This is the chi-squared error, or Mahalanobis distance, between the expected and actual observations. It may be interpreted as the log-probability of $P(k|z)$, where $P(k|z)$ is taken to be a Gaussian with mean $g(z)$ and covariance Ω.

To incorporate these constraints into SLAM, we must know their Jacobian and residual. In this appendix, we enumerate these for various types of sensors, under the assumption that our parameters z store the relative transforms in a pose tree 3.2, as in chapter 3. If z stores poses in a global refrence frame instead, the jacobians are far simpler, and therefore left to the reader to derive.

Weighted jacobians and residuals

As described in 3.3.3, we may split Ω^{-1} into a lower triangular matrix L and its transpose:

$$\Omega^{-1} = LL^T \qquad \text{(B.3)}$$

This allows us to express E not as a Mahalanobis distance, but as a simple norm of a weighted residual:

$$E = \left\| L^T (g(z) - k) \right\| \qquad \text{(B.4)}$$

As in chapter 3, we use the terms "Jacobian" and "residual" to refer to the weighted Jacobian J and weighted residual r, defined as:

$$J = L^T \frac{\partial g(z)}{\partial z} \tag{B.5}$$

$$r = L^T (g(z) - k) \tag{B.6}$$

These may be plugged into (3.7), (3.8), and (3.14) to solve for an exact SLAM update, or into (3.35) for a stochastic H_2O update. In the remainder of this appendix, we present the $g(z)$ and k for all major sensor types, so that they may be used in graphical SLAM.

Position sensors

For position sensors, $g(z)$ calculates some absolute or relative position x, and k is its measured value. The derivative $\frac{\partial x}{\partial z}$ is a $3 \times 7N$ matrix:

$$\frac{\partial x}{\partial z} = \begin{bmatrix} \frac{\partial x}{\partial t_1} & \frac{\partial x}{\partial q'_1} & \frac{\partial x}{\partial t_2} & \frac{\partial x}{\partial q'_2} & \cdots & \frac{\partial x}{\partial t_N} & \frac{\partial x}{\partial q'_N} \end{bmatrix} \tag{B.7}$$

The Jacobian J is also a $3 \times 7N$ matrix, and the residual r is a 3-D vector:

$$\boxed{\begin{aligned} J &= L^T \begin{bmatrix} \frac{\partial x}{\partial t_1} & \frac{\partial x}{\partial q'_1} & \frac{\partial x}{\partial t_2} & \frac{\partial x}{\partial q'_2} & \cdots & \frac{\partial x}{\partial t_N} & \frac{\partial x}{\partial q'_N} \end{bmatrix} \\ r &= L^T (x - k) \end{aligned}} \tag{B.8}$$

If x is a global position, it may be calculated from z using (A.4), and its derivatives $\frac{\partial x}{\partial t_i}$ and $\frac{\partial x}{\partial q'_i}$ are given by (A.11) and (A.24), respectively.

If x is a relative position, we calculate it using (A.38), and its derivatives its derivatives $\frac{\partial x}{\partial t_i}$ and $\frac{\partial x}{\partial q_i'}$ are given by (A.40) and (A.48).

Orientation sensors

Because rotations do not occupy a cartesian space, some care is needed to fit them into our cartesian penalty function $g(z) - k$. Let $r(z)$ be an absolute (A.3) or relative rotation (A.49) as calculated from parameters z, and r_k the same rotation as measured by a sensor. We then let:

$$E = \left\| \pm r(z)^{-1} r_k - q_I \right\|_\Omega \tag{B.9}$$

where q_I is the identity quaternion $\begin{bmatrix} 1 & 0 & 0 & 0 \end{bmatrix}$. In other words, we take the rotation from the calculated orientation $q(z)$ to the measured orientation r_k, and penalize its cartesian distance from the null rotation q_I. This defines $g(z)$ and k as:

$$g(z) = \pm r(z)^{-1} r_k \tag{B.10}$$

$$k = I \tag{B.11}$$

The derivative of $g(z)$ is:

$$\frac{\partial g(z)}{\partial z} = \pm \frac{\partial r^{-1}}{\partial z} \otimes r_k \tag{B.12}$$

$$= \pm \frac{\partial r^{-1}}{\partial r} \frac{\partial r}{\partial z} \otimes r_k \tag{B.13}$$

$$= \pm I^* \frac{\partial r}{\partial z} \otimes r_k \tag{B.14}$$

Plugging (B.11) into (B.6), we get:

$$
\begin{aligned}
r &= L^T k && \text{(B.15)} \\
&= L^T I && \text{(B.16)}
\end{aligned}
$$

Therefore

$$
\boxed{\begin{aligned}
&J = \pm L^T I^* \begin{bmatrix} \frac{\partial r}{\partial t_1} & \frac{\partial r}{\partial q'_1} & \frac{\partial r}{\partial t_2} & \frac{\partial r}{\partial q'_2} & \cdots & \frac{\partial r}{\partial t_N} & \frac{\partial r}{\partial q'_N} \end{bmatrix} \otimes r_k \\
&r = L^T
\end{aligned}} \qquad \text{(B.17)}
$$

The $\frac{\partial r}{\partial t_i}$ terms are filled with zeros, as per (A.27). If r is a global rotation, the $\frac{\partial r}{\partial q'_i}$ derivatives are given by (A.37). If r is a relative rotation, the $\frac{\partial r}{\partial q'_i}$ derivatives are given by (A.53).

Pose sensors

Most sensors used in SLAM give a measure of relative pose, including both the translation and rotaiton. For example, IMU and wheel odometry measure the transform between two consecutive poses, while laser scan-matching and visual feature matching give the transform between two poses with shared observations. For such sensors, $g(z)$ and k are 7-dimensional, with 3 dimensions for position and 4 for rotation. Their position and rotation components are given by the $g(z)$'s and k's for position and rotation sensors, described above. If position and orientation are correlated, this may be expressed in the off-diagonal elements of the 7×7 cvariance matrix Ω. If some components of the pose are left underspecified by the sensor (such as vertical translation for wheel odometry), this can be expressed using high values for the corresponding entries Ω.

The prediction function $g(z)$ and measurement k are given by vertically stacking their position-only and rotation-only counterparts:

$$g(z) = \begin{bmatrix} g_x(z) \\ g_r(z) \end{bmatrix} \tag{B.18}$$

$$k = \begin{bmatrix} k_x \\ k_r \end{bmatrix} \tag{B.19}$$

Here g_x is given by (A.38), g_r by (B.10), k_x is the position measurement, and k_r is given by (B.11). Plugging the above into (B.5) and (B.6), we get:

$$\boxed{\begin{aligned} J &= L^T \begin{bmatrix} \frac{\partial g_x(z)}{\partial z} \\ \frac{\partial g_r(z)}{\partial z} \end{bmatrix} \\ r &= L^T \begin{bmatrix} k_x \\ k_r \end{bmatrix} \end{aligned}} \tag{B.20}$$

The derivatives $\frac{\partial g_x(z)}{\partial z}$ and $\frac{\partial g_r(z)}{\partial z}$ are given by (B.7) and (B.12).

Bibliography

[1] Motilal Agrawal and Kurt Konolige, *Rough terrain visual odometry*, Proceedings of the International Conference on Advanced Robotics (ICAR) (2007). xii, xvii, 6, 10, 15, 19, 20, 21, 23

[2] P Amestoy, H.S. Dollar, J.K. Reid, and J.A. Scott, *An approximate minimum degree algorithm for matrices with dense rows*, Tech. report, ENSEEIHT, 2008. 47

[3] Evan Andersen and Clark Taylor, *Improving mav pose estimation using visual information*, Proc. Intl. Conf. on Intelligent Robots and Systems (IROS), IEEE, 2007, pp. 3745–3750. 8

[4] C. Bibby and I. Reid, *Simultaneous localisation and mapping in dynamic environments (slamide) with reversible data association*, Proceedings of Robotics: Science and Systems (Atlanta, GA, USA), June 2007. 6, 30

[5] Léon Bottou, *Stochastic learning*, Advanced Lectures on Machine Learning (Olivier Bousquet and Ulrike von Luxburg, eds.), Lecture Notes in Artificial Intelligence, LNAI 3176, Springer Verlag, Berlin, 2004, pp. 146–168. 28, 37

[6] Alison Brown and Dan Sullivan, *Inertial navigation electro-optical aiding during gps dropouts*, Proceedings of the Joint Navigation Conference, 2002. 8

[7] Tim Davis, *Direct methods for sparse linear systems*, SIAM, 2006. 47

[8] Timothy A. Davis, *Algorithm 915, SuiteSparseQR: Multifrontal multithreaded rank-revealing sparse QR factorization*, ACM Transactions on Mathematical Software **38** (2011), no. 1. 58

[9] Andrew J. Davison, Ian D. Reid, Nicholas D. Molton, and Olivier Stasse, *Monoslam: Real-time single camera slam*, IEEE Trans. Pattern Anal. Mach. Intell. **29** (2007), no. 6, 1052–1067. 28

[10] F. Dellaert, J. Carlson, V. Ila, K. Ni, and C. E Thorpe, *Subgraph-preconditioned conjugate gradients for large scale SLAM*, IROS, 2010. 30

[11] F. Dellaert and M. Kaess, *Square Root SAM: Simultaneous localization and mapping via square root information smoothing*, Intl. J. of Robotics Research (IJRR) **25** (2006), no. 12, 1181–1204. 36, 47

[12] Martin A. Fischler and Robert C. Bolles, *Random sample consensus: a paradigm for model fitting with applications to image analysis and automated cartography*, Commun. ACM **24** (1981), no. 6, 381–395. 10

[13] Garmin International, Inc., *Gps16/17 series technical specifications*, 2005. 9

[14] Alan George, *Nested dissection of a regular finite element mesh*, SIAM J. on Numerical Analysis **10** (1972), 345–363. 43

[15] M. K. Grimes, D. Anguelov, and Y. LeCun, *Hybrid hessians for flexible optimization of pose graphs*, Proc. Intl. Conf. on Intelligent Robots and Systems (IROS), 2010. xiv, 60

[16] G. Grisetti, R. Kümmerle, C. Stachniss, U. Frese, and C. Hertzberg, *Hierarchical optimization on manifolds for online 2d and 3d mapping*, ICRA (Anchorage, AK, USA), May 2010. 30, 53

[17] G. Grisetti, C. Stachniss, S. Grzonka, and Burgard, *A tree parameterization for efficiently computing maximum likelihood maps using gradient descent*, Proc. of Robotics: Science and Systems (RSS) (Atlanta, GA, USA), 2007. xiii, xiv, 28, 33, 37, 39, 46, 60

[18] Raia Hadsell, Pierre Sermanet, Marco Scoffier, Ayse Erkan, Koray Kavackuoglu, Urs Muller, and Yann LeCun, *Learning long-range vision for autonomous off-road driving*, J. of Field Robotics (JFR) (2009). 19

[19] Chris Harris and Mike Stephens, *A combined corner and edge detector,*, Proceedings of the 4th Alvey Vision Conference, 1988, pp. 147–151. 10

[20] Pinar Heggernes and Pontus Matstoms, *Finding good column orderings for sparse qr factorization*, In Second SIAM Conference on Sparse Matrices, 1996. 47

[21] Christoph Hertzberg, *A framework for sparse, non-linear least squares problems on manifolds*, Master's thesis, University of Bremen, 2008. 53

[22] T.M. Heskes and B. Kappen, *On-line learning processes in artificial neural networks*, Mathematical Approaches to Neural Networks **51** (1993), 199–233. 37

[23] Bernard Hofmann-Wellenhof, Herbert Lichtenegger, and James Collins, *Global positioning system: Theory and practice*, 5th ed., Springer-Verlag, 2001. 9

[24] A. Howard, *Real-time stereo visual odometry for autonomous ground vehicles*, IEEE Int. Conf. on Intelligent Robots and Systems, 2008. 10

[25] Albert Huang, Abraham Bachrach, Peter Henry, Michael Krainin, Daniel Maturana, Dieter Fox, and Nicholas Roy, *Visual odometry and mapping for autonomous flight using an rgb-d camera*, Intl. Symp. of Robotics Research, 2011. 10

[26] M. Kaess, G. Grisetti, and K. Ni, *Automated slam evaluation workshop for 2011 RSS*, `http://slameval.willowgarage.com/workshop/talks/2011-RSS-SLAM-Evaluation.pdf`, July 2011. 54

[27] M. Kaess, V. Ila, R. Roberts, and F. Dellaert, *The Bayes tree: An algorithmic foundation for probabilistic robot mapping*, Intl. Workshop on the Algorithmic Foundations of Robotics, WAFR (Singapore), Dec 2010. 29, 47, 48

[28] M. Kaess, K. Ni, and F. Dellaert, *Flow separation for fast and robust stereo odometry*, IEEE Intl. Conf. on Robotics and Automation, ICRA (Kobe, Japan), May 2009. 10, 21

[29] Georg Klein and David Murray, *Improving the agility of keyframe-based SLAM*, Proc. 10th European Conference on Computer Vision (ECCV'08) (Marseille), October 2008, pp. 802–815. 16

[30] Laurent Kneip, Margarita Chli, and Roland Siegwart, *Robust real-time visual odometry with a single camera and an imu*, British Machine Vision Conference, 2011. 8

[31] K. Konolige, G. Grisetti, R. Kummerle, W. Burgard, B. Limketkai, and R. Vincent, *Sparse pose adjustment for 2d mapping*, IROS (Taipei, Taiwan), 10/2010 2010. 47

[32] Y. LeCun, L. Bottou, G. Orr, and K. Muller, *Efficient backprop*, Neural Networks: Tricks of the trade (G. Orr and Muller K., eds.), Springer, 1998. 28, 37, 38

[33] Mark Maimone, Yang Cheng, and Larry Matthies, *Two years of visual odometry on the mars exploration rovers: Field reports*, Journal of Field Robotics **24** (2007), no. 3, 169–186. 1, 8, 10

[34] Hans Moravec, *Obstacle avoidance and navigation in the real world by a seeing robot rover*, Ph.D. thesis, Stanford University, 1980. 10

[35] David Nistér, Oleg Naroditsky, and James Bergen, *Visual odometry*, Proc. of Conf. on Computer Vision and Pattern Recognition (CVPR) **01** (2004), 652–659. 6, 10

[36] Lauro Ojeda, Daniel Cruz, Giulio Reina, and Johann Borenstein, *Current-based slippage detection and odometry correction for mobile robots and planetary rovers*, IEEE Trans. on Robotics, (TRO) **22** (2006), no. 2. 8

[37] Edwin Olson, *Robust and efficient robotic mapping*, Ph.D. thesis, MIT, Cambridge, MA, USA, June 2008. xiv, 28, 59

[38] Edwin Olson, John Leonard, and Seth Teller, *Fast iterative optimization of pose graphs with poor initial estimates*, Intl. Conf. on Robotics and Automation (ICRA), 2006, pp. 2262–2269. 28, 39, 56

[39] G. B. Orr, *Dynamics and algorithms for stochastic learning*, Ph.D. thesis, Oregon Graduate Institute, 1995. 37

[40] E. Rosten and T. Drummond, *Machine learning for high-speed corner detection*, European Conf. on Computer Vision (ECCV), 2006. 10

[41] Hugh Durrant-Whyte Salah Sukkarieh, Eduardo Nebot, *A high integrity imu/gps navigation loop for autonomous land vehicle applications*, IEEE Trans. on Robotics, (TRO), vol. 15, June 1999. 9

[42] Davide Scaramuzza, Andrea Censi, and Kostas Danilidis, *Exploiting motion priors in visual odometry for vehicle-mounted cameras with non-holonomic constraints*, Proc. Intl. Conf. on Intelligent Robots and Systems (IROS), 2011. 10

[43] H. Schäfer, P. Hahnfeld, and K. Berns, *Real-time visual self-localisation in dynamic environments*, Autonome Mobile Systeme, 2007. 8

[44] Pierre Sermanet, Raia Hadsell, Marco Scoffier, Matt Grimes, Jan Ben, Ayse Erkan, Chris Crudele, Urs Muller, and Yann LeCun, *A multi-range architecture for collision-free off-road robot navigation*, J. of Field Robotics (JFR) (2009). 19

[45] G. Sibley, C. Mei, I. Reid, and P. Newman, *Adaptive relative bundle adjustment*, Proc. of Robotics: Science and Systems (RSS) (Seattle, USA), June 2009. 30, 51, 52

[46] Randall C. Smith and Peter Cheeseman, *On the representation and estimation of spatial uncertainty*, Intl. J. of Robotics Research (IJRR) **5** (1986), no. 4, 56–68. 28

[47] S. Thrun, Y. Liu, D. Koller, A.Y. Ng, Z. Ghahramani, and H. Durrant-Whyte, *Simultaneous localization and mapping with sparse extended information filters*, Intl. J. of Robotics Research (IJRR) (2004). 28

[48] Sebastian Thrun, *Exploring artificial intelligence in the new millennium*, ch. Robotic mapping: a survey, pp. 1–35, Morgan Kaufmann Publishers Inc., San Francisco, CA, USA, 2003. 6

[49] Michael Veth and John Raquet, *Two-dimensional stochastic projections for tight integration of optical and inertial sensors for navigation*, National Technical Meeting Proceedings of the Institute of Navigation, 2006, pp. 587–596. 8

[50] Matthew R. Walter, Ryan M. Eustice, and John J. Leonard, *Exactly sparse extended information filters for feature-based slam*, Intl. J. of Robotics Research (IJRR) **26** (2007), no. 4, 335–359. 28

[51] Chris C. Ward and Karl Iagnemma, *Classification-based wheel slip detection and detector fusion for outdoor mobile robots*, Intl. Conf. on Robotics and Automation (ICRA), IEEE, 2007, pp. 2730–2735. 9

[52] ______, *Model-based wheel slip detection for outdoor mobile robots*, Intl. Conf. on Robotics and Automation (ICRA), IEEE, 2007, pp. 2724–2729. 9, 16

[53] Mark D. Wheeler and Katsushi Ikeuchi, *Iterative estimation of rotation and translation using the quaternion*, Tech. Report CMU-CS-95-215, Carnegie Mellon University, December 1995. 75